Research Article
Journal of Geophysical Research: Oceans
DOI 10.1002/2017JC013003

Pancake ice thickness mapping in the Beaufort Sea from wave dispersion observed in SAR imagery

P. Wadhams[1,2], G. Aulicino[2], F. Parmiggiani[3], P. O. G. Persson[4], and B. Holt[5]

[1] Cambridge Polar Consultants Ltd., Cambridge, UK.

[2] Università Politecnica delle Marche, Ancona, Italy.

[3] ISAC-CNR, Bologna, Italy.

[4] University of Colorado at Boulder, Colorado, USA.

[5] Jet Propulsion Laboratory, California Institute of Technology, Pasadena, California, USA.

Corresponding author: Peter Wadhams (email p.wadhams@damtp.cam.ac.uk).

Key Points:

- Sea ice thickness – we describe and thoroughly test a technique which derives thickness from wave dispersion changes.
- Pancake ice – is the ice type concerned, in which waves propagate according to a viscous dispersion model.
- SAR (synthetic aperture radar) images enable the wavelength changes due to the ice to be measured.

This article has been accepted for publication and undergone full peer review but has not been through the copyediting, typesetting, pagination and proofreading process which may lead to differences between this version and the Version of Record. Please cite this article as doi: 10.1002/2017JC013003

Received: Apr 18, 2017; Revised: Dec 15, 2017; Accepted: Jan 18, 2018

Abstract

The early autumn voyage of RV *Sikuliaq* to the southern Beaufort Sea in 2015 offered very favourable opportunities for observing the properties and thicknesses of frazil-pancake ice types. The operational region was overlaid by a dense network of retrieved satellite imagery, including SAR (synthetic aperture radar) imagery from Sentinel-1 and COSMO-SkyMed (CSK). This enabled us to fully test and apply the SAR-waves technique, first developed by Wadhams and Holt [1991], for deriving the thickness of frazil-pancake icefields from changed wave dispersion. A line of sub-images from a main SAR image (usually CSK) is analysed running into the ice along the main wave direction. Each sub-image is spectrally analysed to yield a wave number spectrum, and the change in the shape of the spectrum between open water and ice, or between two thicknesses of ice, is interpreted in terms of the viscous equations governing wave propagation in frazil-pancake ice. For each of the case studies considered here, there was good or acceptable agreement on thickness between the extensive *in situ* observations and the SAR-wave calculation. In addition, the SAR-wave analysis gave, parametrically, effective viscosities for the ice covering a consistent and narrow range of 0.03 to 0.05 m^2s^{-1}.

1. Introduction

The polar regions are distinctly different from other geographic areas and share a common set of characteristics, including remoteness; limited accessibility; low population densities; sensitive ecosystems of global importance; rich non-renewable (hydrocarbons, minerals) and renewable (fisheries, forestry) resources; and increasing industrial activity. In recent years, the uniqueness of these polar regions and their importance to the world has been recognized, and efforts have been made to develop policies in a cooperative manner across regions and nations. This is made more urgent by the fact that the Arctic is warming much more rapidly than other parts of the world, and the summer sea ice is thinning and shrinking significantly. Such physical change in a remote area can best be monitored by remote sensing from space. Although a number of satellite derived approaches exist for estimating sea ice properties [Aulicino et al. 2014], many of them are often limited to a certain sea ice thickness range, type and/or region [Cerrone et al., 2017]. In every case the data provided by the many types of sensors must be validated by ground truth.

Here we report on the analysis of satellite SAR data obtained over the operational area of a research cruise in the southern Beaufort Sea in September-November 2015. Preliminary results can be found in Wadhams et al. [2016], and the cruise itself is described in Wadhams and Thomson [2015]. Spectral analysis of the images yields the directional wave spectrum of the ocean, and since the dispersion relation is altered by the presence of small floating ice particles – i.e. frazil and pancake ice – a model of the way in which floating ice affects wave dispersion can, in principle and practice, yield a thickness for the frazil-pancake icefields. In turn the ship's sampling activities provided extensive ground truth for the study. The cruise concerned was an autumn operation by RV *Sikuliaq* (University of Alaska) in a project funded by the Sea State initiative of the US Office of Naval Research; P. Wadhams, P. O. G. Persson and B. Holt were

aboard the ship. SAR data from a number of sensors were made available to the ship, including CSK data requested by F. Parmiggiani, and have been compared with *in situ* observations on the extensive pancake icefields encountered, including information on the thickness and size of the pancakes and the spectrum of waves passing through them as measured by directional wave buoys.

The aim of the study was to build on a relationship between frazil-pancake (FP) ice layer thickness and changed ocean wave dispersion, a relationship which was originally described by Wadhams and Holt [1991] and experimentally verified by Wadhams et al. [2004]. Wadhams and Holt showed that two-dimensional wave number spectra calculated from Seasat SAR imagery could be used as the source of the wave dispersion information. Pancake ice gives a dark return on SAR imagery because of the way in which it damps out very short (a few cm wavelength) ripples at the Bragg wavelengths, but it still permits longer ocean waves to show through and thus be detectable in spectral analysis.

Frazil and pancake ice are two of the most important sea ice types in the world ocean, yet their role in the energy system of the cryosphere has been little studied. Frazil ice forms when seawater freezes in turbulent conditions such as an open ocean with a wave field, and consists of a suspension of crystals which gives the sea a milky or oily appearance and damps down waves. As freezing continues, the frazil crystals crowd together and finally freeze together in groups to form small cakes. Wave action prevents the cakes from freezing together to create a continuous ice cover, and causes collisions which maintain the cakes as separate, semi-circular entities. However, the collisions also pump frazil ice over the cake edges during impact. The result is a series of cakes with raised rims (hence the resemblance to pancakes) which may achieve eventual diameters of up to 5 m and thicknesses of up to 75 cm in areas where they have a long lifetime with constant exposure to waves (e.g. Odden ice tongue in the Greenland Sea, Wadhams and Wilkinson, 1999).

More usually, pancake ice appears only temporarily at an advancing ice edge and may reach thicknesses of only a few tens of cm and diameters of 1-3 m. The associated high salt flux gives frazil-pancake (FP) ice a significant geophysical and climatic importance. Some relevant aspects are:

1. FP forms the outer part of the Antarctic ice cover in winter, and the ice edge advances by growing new pancake ice; further from the edge, where wave action is damped, the cakes freeze together to create consolidated pancake ice, which is the basis of about 40% of the Antarctic ice cover [Wadhams et al., 1987]. The southern Beaufort Sea in autumn also constitutes an ice edge advancing into water subject to a wave field, so here too one expects fields of FP ice to form, and this was observed by *Sikuliaq.*

2. FP is the main ice type where coastal polynyas are kept open by prevailing offshore winds. The consequent salt flux can enhance the vigor of the overturning process in the polynya. This makes polynyas a major source of bottom water in the Antarctic [Jacobs, 2004; Sansiviero et al., 2017], but they also play an important role along certain Arctic coasts, such as Alaska (Norton Sound, St Matthew Island, St. Lawrence Island, Point Barrow, and Banks Island) where their existence is very important for the livelihood of indigenous people.

3. FP plays a role in shelf-slope convection by which mid-level water masses are renewed in early winter at the Siberian shelf edges and in the Sea of Okhotsk [Kinney et al., 2009].

4. In the sub-Arctic seas an important location for pancake ice is the Odden ice tongue in the central Greenland Sea, at about 75ºN 0ºW. Here FP ice grows locally in the cold water of the Jan Mayen Polar Current over a site where in winter salt rejection causes the surface water to become more dense, to overturn and sink, and hence to create one of the few regions of open ocean convection in the world ocean. This is a place where the famous "chimneys" have been discovered, long-lived rotating columns of sinking water [Morawitz et al., 1996; Wadhams et al., 2004b]. Cessation of pancake ice production would reduce the intensity of the entire Atlantic meridional overturning circulation, which would cause cooling (or reduced warming) of the Atlantic seaboard of Europe, particularly the UK and Ireland but also western France and Norway [Christensen and Christensen, 2007].

Thus FP ice plays two main geophysical roles: assisting convection through enhancement of salt flux, and being the basis for a growth cycle which contributes disproportionately to the annual mass budget of the sea ice in critical regions. Hence its area and effective thickness are key parameters.

The seminal paper by Wadhams and Holt [1991] started a new area of research which is now coming to maturity, through application of the technique that they proposed to the systematic determination of mass budgets. Wadhams and Holt showed that: i) ocean waves passing through FP icefields are still visible on SAR imagery although the ice-covered areas give a dark return because of suppression of wave energy at the very short Bragg wavelengths; ii) the wavelength of a wave crossing an ice edge is shortened, indicating that the dispersion relation for waves in ice differs from open water, the difference being capable of analysis to yield the thickness of the icefield.

The technique takes a SAR image and uses spectral analysis of a line of subscenes within the image to map the change in the wave spectrum as waves enter a pancake icefield (with the advancing wavefront corresponding to the major axis of the line of subscenes), then uses a theoretical relationship between ice thickness and wave dispersion to calculate the pancake thickness. This can be applied to all icefields where pancake ice fringes open water, e.g. the Antarctic ice edge; the Odden ice tongue in the Greenland Sea; the Bering-Chukchi seas; and now, in autumn, the southern Beaufort Sea.

After initial studies which extracted a wave number spectrum from the SAR image without correction [Wadhams and Holt, 1991], modern work began with conversion of the raw SAR spectrum into a valid sea surface directional spectrum using two correction techniques, the Hasselmann inversion [Hasselmann et al., 1996] and the cross-spectra inversion [Engen and Johnsen, 1995]. Using these methods the directional spectrum in open water and in nearby frazil-pancake ice could be found by analysis of subscenes from a single image [Wadhams et al., 1999, 2002]. By tracking the peak of the spectrum through a succession of subscenes as the waves move into the icefield, and measuring the change in wave number of this component on crossing the ice edge, we were able to estimate the ice cover thickness through use of thickness-dependent dispersion theory. The method was still further improved by dealing with the whole shape of the spectrum, not just the dominant peak.

Initially a mass-loading theory [Keller and Weitz, 1950] was used to model wave dispersion in pancake ice [Wadhams, 1986], but this predicted greater ice thicknesses than are actually observed during the field campaigns. Since then we found that a later model, also by Keller [1998], in which the FP ice cover is treated as a layer of highly viscous fluid, offered a better description of wave dispersion and attenuation, which could give us a new means of obtaining more accurate thickness estimates. Thus, a new model based on viscosity was developed and tested successfully against physical retrievals of pancakes from the Antarctic marginal ice zone [Wadhams et al., 2004]. It is this model which we here subject to much more extensive testing against the superb observational dataset procured by *Sikuliaq*. The small diameters of pancakes in relation to wavelengths allow us to ignore the elasticity of the cakes. We note that recently a two-layer viscous model has been proposed [Doble et al., 2015] in the context of calculating wave decay rates in pancake icefields, but we believe that the additional complication of adding a somewhat arbitrary viscous water layer under the ice does not improve the retrieval of sea ice thickness.

FP ice thickness as obtained from SAR analysis and models needs to be validated at natural ocean scales by field experiments with ground truth. The *Sikuliaq* cruise, which performs this function for the data in this paper, achieved the following:

1. Collection and analysis of pancakes and frazil under the path of a SAR satellite so as to test the validity of thickness predictions made by the SAR-wave method;
2. Independent estimations of ice thickness from visual bridge observations using the Arctic Shipborne Sea Ice Standardization Tool - ASSIST protocol (http://icewatch.gina.alaska.edu/pages/about) and from local application of a thermodynamic technique in conjunction with direct surface energy flux measurements [Wang et al., 2010; Persson et al., pers. commun.].

3. Measurement of the wave spectrum within the pancake icefield, which will be used to measure the rate of wave decay within the frazil-pancake zone and understand the dynamics governing the spatial variability of frazil-pancake thickness and ice production rates.

Section 2 describes the methodology for retrieving ice thickness from the SAR spectra. In section 3, we describe relevant details of the *Sikuliaq* cruise, and report on and discuss the SAR FP ice thickness retrieval and its validation for four 1-4 day experiment periods during the Sea State cruise. These are October 10-13, 16-18, 23-24, and October 31 - November 1, 2015.

2. The use of SAR to retrieve pancake ice thickness

A basic requirement of our task was the availability of SAR imagery in conjunction with the *Sikuliaq* field campaign. Until recently earth observation (EO)-based sea ice detection has been done using Envisat/ASAR images, but in April 2012 the Envisat satellite ceased to operate and is currently substituted by two families of SAR satellites: ESA Sentinel-1 (hereafter S1) and COSMO-SkyMed (CSK) of the Italian Space Agency (ASI). S1 images have open access through the ESA Scientific Data Hub archive, while CSK images must be purchased through the ASI web site. Other SAR products may well be appropriate for this method, i.e. RADARSAT-2 (RS2) and TerraSAR-X, but during the experiment the extensive collection of RS2 imagery was obtained in a mode where the resolution was too coarse for wave imaging, and no TerraSAR-X images were obtained with the correct location and timing needed for this particular application.

For S1 one must retrieve what can be found in the archive, while CSK images can be ordered for exactly the area and the date for which one is interested. This is a very important advantage in the case of field campaigns in the Arctic. The CSK SAR constellation also offers a unique revisit capability (i.e. up to 16 acquisitions/day over a specific target at 70°N latitude) and rapid access that can support activities such as near-real time icebreaker requirements for maritime safety and transportation activities during winter navigation, and oil and gas exploration activity monitoring. In addition, CSK satellite imagery with X-band SAR allows better detection, measuring and tracking of ice floes on a daily basis, than the S1 C-band SAR is able to provide; it also gives better information on the size and movement of potential ice features, as well as increasing the ability to forecast their movements. Both sensors obtained imagery at a resolution (less than 25 m) suitable for wave detection.

Thus, for our purposes, we opted to use the HH-polarized images collected by the CSK SAR-X sensor during the *Sikuliaq* field activities (the 11th, 17th, 24th October and 1st November 2015) and distributed by e-GEOS, a joint venture of ASI. We also used the available S1 SAR-C images co-located with the experiments done on the 1st November 2015.

The analysis of the SAR images followed the procedure described in Wadhams et al. [2002, and especially 2004] making use of ESA-NEST, TerraScan and MATLAB software packages and

the RSI Interactive Data Language. First, a strip of several imagettes, or subscenes, is extracted from the SAR scene across the ice/sea edge in the proximity of the *Sikuliaq* pancake measurement locations, following the main direction of the incoming waves; the size of each subscene window is 512x512 pixels, i.e. 7.68 x 7.68 km and 10.24 x 11.26 km for the CSK and S1 data, respectively (~ 15 m and 20 m resolution, respectively). The imagette SAR spectrum is then computed, providing the input to the following SAR/wave spectrum inversion step together with the wind speed values measured along the *Sikuliaq* track during the experiments. For the open sea windows (see Appendix A), the inversion procedure utilizes the observed *in situ* wind speed to derive the best wave age value, defined as the ratio between wind speed and the phase velocity of the dominant wave, which minimizes the differences between the observed SAR spectrum and that inferred using the Hasselmann and Hasselmann [1991] integral transform as improved by Hasselmann et al. [1996]. For the pancake ice subscenes (Appendix B), a wave propagation model following Keller [1998] viscous theory, which accounts for wave dispersion and attenuation as a function of wave number and ice properties, is used to invert the SAR spectra and compute, again parametrically, the pancake ice thickness and the wave attenuation rate. The change in the shape of the spectrum when the waves enter the ice is usually very clear, as shown by the experiments' results reported in the following section.

3. The *Sikuliaq* cruise experiments and their results

In autumn 2015 (September 30 - November 10) the University of Alaska research ship *Sikuliaq* worked in the marginal ice zone of the Beaufort Sea, to study the processes which govern the advance of the Arctic Ocean ice edge in autumn. The cruise is described by Wadhams and Thomson [2015]. During several experiments, a line of wave buoys was deployed along a pre-declared track, which could thus be covered by simultaneous CSK or other SAR images. In this section we describe an analysis of the images during four experiments, which covered an area where frazil-pancake ice was the dominant ice type along the entire length of the survey line out to open water. The ground truth facilities deployed included: i) directional wave buoys (WB) placed in the water between pancakes; ii) SWIFT (Surface Wave Instrumented Float with Tracking) directional wave buoys placed outside of the ice edge; iii) measurements of pancake ice thickness by recovery of cakes from over the side and of frazil ice mass per unit area using a collector (frazilometer) giving a sample that is allowed to melt out; iv) visual pancake ice thickness observations collected from the *Sikuliaq* bridge following the ASSIST protocols; v) 10-minute average ice thickness estimates based on a thermodynamic technique utilizing surface temperature and energy flux measurements from the ship [Yu and Rothrock, 1996; Wang et al., 2010; Persson et al., pers. commun.]; vi) wave height measured from a 1-D lidar mounted on the bow mast of the ship; vii) direction of the dominant waves from the shipboard marine radar [Lund et al., 2017], and viii) basic meteorological measurements from instruments on the bow mast [Thomson et al., 2015].

Direct sampling of the ice was carried on throughout the voyage whenever the ship stopped or slowed, and was carried out 24 hours a day. At each stop two or more pancake ice samples were collected by an over-side landing net. Whole cakes were lifted onto the deck, their dimensions (diameter, thickness) were immediately measured and the cake was then cut up for salinity analyses. Frazil ice was sampled by a frazilometer, a tube closed at one end by fine mesh, which was lowered below the surface and pulled up through the frazil layer so that the volume of frazil collected could be converted into a volume per unit area of sea surface (equivalent to a thickness). Sea water was allowed to drain out of the frazilometer and the sample was then collected in a plastic bottle. During the early days of the cruise when the ice consisted of small pancakes embedded in frazil, this brought in representative whole pancakes, but later the cakes sampled were the smaller cakes or fragments of ice broken up by the ship's reamer. In every case efforts were made to obtain samples that were as representative as possible of the visually observed dominant thickness nearby, and sometimes more than one sample was taken with the results collected in different bottles according to thickness.

Visual ice observations were made every hour from the bridge while underway and logged using the internationally-agreed ASSIST protocols. The small scale of the pancakes, ice cakes and brash (meters to tens of centimeters) are well below the resolution of satellite radar images. Occasional ground truth from sampling is noted in the record whenever possible. Observations were divided into pancake ice, multiyear ice and other forms (consisting mostly of nilas and broken young ice forming into brash and small cakes). A previously unreported finding for this region from this cruise is the widespread occurrence of newly forming pancake ice.

The thermodynamic technique as utilized from satellite measurements is described by Yu and Rothrock [1996] and Wang et al. [2010] but has been adapted to be used with measurements available from a research vessel by Persson et al. (pers. commun.). The scheme assumes 1) an energy flux balance between the conductive flux and the net energy flux to the atmosphere at the surface of the ice, 2) that the conductive flux is constant through the depth of the ice, and 3) that there is no snow on the ice or that the snow thickness is known. It then utilizes direct measurements of the surface skin temperature and net surface energy flux to back out the ice thickness that corresponds to the observed energy flux. When applied on a large scale from satellites, Wang et al. [2010] found satisfactory agreement between this methodology and submarine sonar ice thickness measurements. Persson (pers. commun.) has found variable success with the technique when applied on a much smaller scale from the *R/V Sikuliaq*, with thicknesses frequently in agreement with or slightly thicker than the direct dipnet measurements but often thinner than those obtained from the visual observers. This technique yielded thickness estimates at 1 Hz temporal resolution (averaged to 10 minutes) throughout the entire cruise. Only at times when both IR skin temperature sensors were covered with rime icing did this method fail to obtain a thickness estimate. Evaluation of this technique is ongoing.

Indirect sampling of sea ice thickness through electromagnetic induction sounding (EMI) and ranging techniques was carried out with a SIMS (Sea Ice Measurement System) rig suspended on the aft port crane during most underway transits from October 5th to 23rd. Considerable difficulties were encountered in interpreting SIMS data for pancake ice areas because of their free water content, so this method of validation has not been utilized.

A total of 32 days (559 hours) of visual ice observations, 228423 ice camera images and 467 physical ice samples were collected during the *Sikuliaq* research voyage. Among these, only the data co-located in space and time (± 12 hours) with available CSK and S1 images have been included in our analyses.

The wind data used in this study were collected from a sonic anemometer on the 16.5 m-tall bow mast of the *R/V Sikuliaq* and supplemented with data from two other anemometers on each side of the ship's superstructure at times when the ship-relative wind direction was from the stern. Significant quality control analysis was done to combine the data into a high-quality data set. The 1-D Riegl lidar was also mounted near the top of the bow mast, providing a distance to the ocean surface every 0.5 s, which was combined with ship-motion measurements to obtain wave heights at 2 Hz temporal resolution. 10-minute significant wave heights are computed as four times the square root of the 0-th moment of the motion-corrected distance spectra (moment technique) and as four times the standard deviation of the distances (CF method). The first method is more accurate but requires that at least 50% of the samples during the 10-minute time period are available, while the latter can obtain reasonable values with more missing data. Icing on the optics was the major reason for missing data. The direction from which the peak waves are coming (wave direction) are obtained from analysis of the marine radar backscatter fields [Lund et al, 2017]. The radar was mounted on the main mast of the ship.

3.1. Experiment of 10-13 October 2015

The field operation of 10-13 October was set up as a major swell arose and passed through the pack in a zone of pancake ice. On October 10th, SWIFTs and WBs (Cambridge wave buoys) were deployed to drift in an array aligned perpendicular to the primary wave fronts that were forecast to come in from the open water from the E and SE during the rising storm. The experiment was located along the SE side of the ice edge in the Beaufort Sea where pancake ice had been forming rapidly for same days. Significant wave heights in the open water on Oct 10 were 0.4-0.5 m (Fig. 1c, 5-10 UTC Oct 10), but rapidly increased to over 4 m on Oct 11 and stayed at that height for 36 h as the winds increased to 15-17 m/s from the east-southeast (Fig. 1a, 1b). The peak waves were initially from the SE but gradually changed to be from ESE. Figure 2a shows the location and backscatter from the SAR image at 1434 UTC Oct 11, while the AMSR2 ice concentration images (Fig. 2b,c) show that the ice imaged by the SAR on Oct 11 was sampled by the ship on Oct 10 between 12 UTC and 23 UTC. Figure 3 (top to bottom) shows photographs taken on Oct 10 illustrating the ice conditions at the approximate locations of

imagettes 2, 4, and 5, respectively, 14-19 h before the SAR image was acquired. The pancake sampling on Oct 10 showed that typically they were about 30 cm in diameter, very weak and of thickness only 2.4±0.8 cm. These sample thickness estimates were in good agreement with the other thickness estimates of 2-10 cm (see Fig. 1d at 12-22 UTC Oct 10). Further buoy lines were laid out across the ice edge to the north (Fig. 2) on Oct 10, then as the fetch for this northern line became limited, a second line of buoys 120 km in length was laid out along the ship track further to the south from open water to deep within a field of growing pancakes. This southern line was mostly outside the SAR image to be analyzed. Direct sampling along the southern line on Oct 11 reported thicknesses ranging from 4 cm to 12 cm and diameter values from 18 cm to 78 cm with much evidence of rafting (Fig.1d).

The expectation was for the pancake ice to eventually freeze in place as the storm died down. However, the ice concentration within the SAR image domain decreased from Oct 10 to 11, and ice was nearly absent from the domain by Oct 12 (Fig 2b, 2c, and 2d). Pancakes along the southern line largely disappeared overnight from Oct 11 - 12 in the immediate vicinity of the buoy array, while the waves reached a maximum of 5 m in the middle of the array on Oct 12 (Fig. 1c), which was now near the SE edge of the ice (Fig. 2d). Further to the west and south, the ice concentration increased from this event. The working hypothesis is that the waves provided sufficient mixing to release the ocean heat stored in the near surface temperature maximum observed with the underway CTD [Smith et al., pers. commun.]. This means that pancake ice forms in the first place because of wave action but can also be destroyed by excessive wave action which brings up ocean heat stored during the summer. The waves may not have penetrated into the ice farther to the west, so heat loss to the atmosphere dominated and instead enhanced the ice concentration there during this event. Alternatively or in addition, floe convergence increased the ice concentration in these regions. The buoys were recovered on Oct 13.

In order to cover this experiment, the acquisition of a SAR-X CSK satellite image over the area of the field operations gave us the state of the region for October 11th at 14:34:09 UTC (Fig. 2a). At this time a wind speed of 14 m/s was measured aboard the ship, and the wind direction had been steady from the east for 36 h (Fig. 1a,b). Ice concentration had decreased from that of Oct 10, and it is possible that the ice thickness along the northern transect may have decreased somewhat from that measured on Oct 10. Inversion procedures were applied to both the open water and the sea ice SAR spectra for five imagettes of the extracted stripmap (Fig. 2a); the change in shape of the spectral peak region when the waves enter the ice (Fig 4) is very apparent. Please note that in this and all subsequent stripmaps and displayed directional spectra the “top” of the map or spectrum is not due north but a direction at right angles to the incoming major wave vector.

Most of the shorter wavelengths are damped by the FP ice cover, which results in a cleaner, clearer wave spectrum within the ice cover than in the open ocean. From these data a pancake ice

thickness of 21.4±1.0 cm was retrieved (error bars are the inherent error in the spectral comparison method) together with a kinematic viscosity of 0.05 $m^2 s^{-1}$, the latter being consistent with the values previously derived from tank experiments [Newyear and Martin, 1999]. This value looks reasonable for a pancake thickness icefield, though it is higher than both the thickness of single pancakes recovered manually by net sampling over the ship side (Fig. 5) and the regional mean pancake thickness measured by visual observations and the thermodynamic technique (ranging from 2.9 cm to 11.9 cm) (Fig. 1d), especially if one allows for some melt of the ice cover between the time of the shipboard ice thickness observations and the SAR acquisition. The difference is that photographs of the region during that day (e.g. Fig. 3d, image 3642 from *Sikuliaq* data file, taken 1953 UTC on Oct 11) show two layers of pancakes; an upper layer, with upturned edges, resting on a lower layer of flooded pancakes, like upside-down saucers: the lower layer pancakes are probably overturned, but may simply have had their rims washed off. The effective thickness of the icefield, in terms of volume per unit area of sea surface, is therefore roughly double the thickness of a single pancake. The useful implication here is that the SAR-waves technique may be giving a higher, but more accurate, picture of ice volume than the sampling of single pancakes would offer.

Note that the inverse procedure [Wadhams et al., 2004] is parametric because the best fit analysis for the spectra yields *both* ice thickness *and* kinematic viscosity.

3.2. Experiment of 16-17 October 2015

Upon reaching the ice edge on the Chukchi Sea side, a diffuse edge with small pancakes was found on October 16th. During the last 9 h of Oct 16 and the first 8 h of Oct 17, the winds were from the west at 2-5 m/s (Fig. 6a,b). The incident waves came from the west and southwest, with significant wave heights of up to 60 cm (Fig. 6b,c), and a line of buoys, perpendicular to the ice edge, was deployed at this site while the ice was advancing rapidly towards the southwest. The seaward boundary was characterized by pancake ice mixed with frazil ice and several huge and medium sized pieces of multi-year ice heaving amongst the cakes (Fig. 7). On the 17th small sub-mesoscale eddies appeared in this region, detected by loose pancake ice being driven by underlying eddy current patterns. Direct sampling showed the presence of dense, thick pancake ice overlapping large darker pancakes. The eddy activity may have been related to the fact that the ice edge lay over the shelf break, where a current jet can be expected.

A SAR-X CSK image was acquired over the area on October 17th at 13:58:33 (Fig. 8). By this time the winds had reversed direction and were now weakly from the east (Fig. 6b). The 1-D significant wave heights were 30-50 cm at the time of the off-ice location of the ship (near 12 UTC Oct 17), and the marine radar peak wave direction [Lund et al., 2017] was 190°-214°, so swell persisted from the SSW even after the wind direction had shifted. The inversion procedure was applied to open water and sea ice subscenes extracted from the SAR stripmap (Fig. 8) including the field activity locations, with a wind speed of about 3 m/s. Figure 9 shows the open

water and the sea ice SAR spectra. Pancake ice thicknesses of 8.1±1.0 cm, 10.4±1.0 cm and 13.0±1.0 cm were retrieved for imagettes 3, 4 and 5, respectively; again, the kinematic viscosity parametrically retrieved through the model was 0.05 m^2 s^{-1}. These results agree well with *in situ* observations which ranged from 4.9 cm to 10.2 cm near the ice edge at the time and location of the SAR imagette acquisitions (Fig. 6d), but extended up to 20-30 cm when the ship was farther from the ice edge before and after this time. The retrieved thicknesses are higher than thickness measurements obtained from the single pancake sampling activities (Fig. 6d, Fig. 10) which gave average thickness values of 5.7±2.3 cm, 6.0±2.9 cm and 8.3±2.4 cm in the three sub-regions.

Another wave experiment was carried out on the following day, 18th October. Unfortunately, no CSK images were available that day covering the area of field activities. Nonetheless, the site of *Sikuliaq* field activities was still observed by the previous day SAR image, so we decided to use it to retrieve the pancake ice thickness. Although the presence of an eddy made the ice spectra somewhat noisy, a value of 12.1±1.0 cm was retrieved for the subscenes where the field measurements gave thicknesses ranging from 7.7 cm to 13.1 cm (Fig. 11).

3.3. Experiment of 23-24 October 2015

The purpose of this experiment was to measure wave reflection and propagation in a field of pancakes which may be large enough to cause scattering as well as, or instead of, viscous propagation. A line of buoys extending from 20 km within the pack ice out to open water was deployed on 23rd October. Bands of pancakes were forming. The onboard marine radar showed a clear straight ice edge running NW-SE along 130°-310°, at right angles to our outward course. Drift patterns suggested strong eddies at the shelf-break, and the buoys were alternately drifting in and out of bands of ice consisting of small thin fragments of nilas which had been broken up by the waves. Pancake ice samples disturbed by the ship ranged from 3 cm to 5 cm thick at the ice edge in approximate agreement with the other thickness estimates (see Fig. 12d at 16-18 UTC Oct 23), though bands of significantly thicker ice (up to 10-30 cm) existed only a few tens of kilometers farther into the ice. A zone of concentrated but loose pancake ice was then found and further inside the ice, in a small area of open water, a complete ice cover of very thin cemented pancakes, typically 3 cm thick and almost transparent. At the ice edge and over the adjacent open water, winds were from the ESE at 10-12 m/s. The wind produced significant wave heights of about 1 m in close proximity to the ice edge and up to 2.5 m a little farther off-ice, with the wave direction being parallel to the ice edge (Fig. 12c,d).

On 24th October a patch of pancake ice made of individual large pancakes was found at 19-24 UTC; five pancakes and many fragments were sampled, so we had a good dataset on pancake thicknesses in this zone. The other component of the icefield was brash, there being no frazil present.

To carry out the SAR analysis in this experiment we used a CSK image obtained on October 24th at 15:16:24 (Fig. 13). The zone of pancake ice is clearly visible as a darker tone, while individual ice floes show up as white targets. The wind speed was about 11 m/s at the time of the SAR retrieval. For our analysis, a stripmap of six imagettes was extracted across the ice/sea edge in the proximity of the pancake sampling positions.

The SAR spectrum computed for each ice or open water imagette was used as input for the application of the inversion procedure described above. Figure 14 shows the SAR-derived wave spectra in open water and ice which provided a pancake thickness of 16.3±1.0 cm and 17.8±1.0 cm in sub-scenes 5 and 6 respectively (kinematic viscosity ranging between 0.03 and 0.04). The spectral peak orientation showed that a wave field was obliquely entering the ice. These estimations show a lower agreement with both ASSIST visual and the thermodynamically-derived thickness observations (average value of 5.6±0.6 cm) and pancake direct measurements (6.7±1.9 cm on average, with a maximum thickness of 10.5 cm) collected during the buoy operations right at the ice edge, but are in reasonable agreement with the thicknesses measured just a little farther from the ice edge, as described above and in Figure 15. Nonetheless, these results may be relevant to the presence of several big floes in the pancake icefield, as shown by the SAR image especially in Figure 14c for imagette 6; these would add a thick ice component to the area-averaged thickness, and also may have a further effect in causing some wave energy to be scattered rather than to propagate according to the viscous equations. It is also possible that, as in the experiment of October 11, the pancake icefield was compressed so that it was effectively double-layered, increasing the real ice mass per unit area to a greater figure than suggested by single pancake thicknesses.

3.4. Experiment of 31 October - 1 November 2015

This experiment was conducted on the western side of the advancing ice edge, in a region where the ice edge corresponded in location to the shelf break, with associated strong shelf edge current shear. Oceanographic factors played a large role in the ice dynamics during the experiment. It was also an icefield that, for the first time in the cruise, was composed of small ice floes rather than pancake ice, the floes seeming to have a pancake origin but with the cakes cemented together and then re-broken, so that the average floe diameter was 10-20 m. This was large enough for scattering to be a mechanism of wave-ice interaction rather than purely dispersion change due to addition of a viscous layer. Therefore it was of special interest as possibly marking the limit of validity of wave-ice dispersion as a method of thickness estimation.

Winds were first on-ice and mostly weak, first from the SSE and later from the W (Fig. 16a,b). Late on Oct 31, the wind again changed to be from the southeast and south, gradually increasing in speed on November 1 as it backed to ESE and then E. At the time of the SAR overpasses (1547 UTC and 1723 UTC Nov 1), the ESE winds of 10 m/s had a significant off-ice component.

When the ship was in open water near the ice edge on Nov 1, significant wave heights were 1.1-1.3 m (Fig. 16c).

When we arrived at the first ice on October 31st, the ice was a very dilute sporadic soup of small pancakes, frazil and brash in various strips and bands, gradually increasing in density. Then, we moved to bigger pancakes, increasing in concentration to 100%. In the darkness it made the icefield look distinctly whiter and really did mark a line separating pancakes from bigger floes, themselves cemented pancakes. Wave buoys were deployed along the boundary between pancake and small floes and ice samples were collected, obtaining fragments of pancake of thickness ranging from 3 cm to 14 cm. The continuous ice thickness observations showed areas or bands of very thin (3-5 cm) ice interspersed with areas of ice 10-30 cm thick (see Fig. 16d from 15 UTC Oct 31 to 7 UTC Nov 1). Near 07 UTC, a sharp ice edge into open water was crossed, a sudden transition from a complete cover of cemented pancakes, with no visible swell, to completely open sea, with just the outer fringe being more broken up. Near daybreak on November 1st (~20 UTC) wave buoy recovery was accompanied by an overside pancake sampling, showing the range of ice thicknesses in the region as summarized in Table 1 and seen in Fig. 16d. Later in the day a very compact ice edge was crossed, composed of small newly formed pancakes in an overlapping fish scale pattern. Then pancakes got bigger when passing into the main pack made of a tight cover of pancakes but without clear bands.

A CSK SAR-X image was obtained on November 1st at 15:46:37 in the area covered by the buoys and is shown in Figure 17. The observed wind speed was 10 m/s from ESE (obliquely off-ice) at the time of the SAR passage; however, the marine radar indicated that the swell direction (peak wave direction) was from 225° (Fig. 16b). Two strips of four 512x512 pixels imagettes were extracted across the ice/sea edge in the vicinity of the buoy positions and pancake thickness was derived, through the application of the inversion technique described above. Figure 18 shows the SAR spectra computed for ice and open water imagettes of both stripmaps which provided the input to the inversion step for deriving the ice thickness. Again a change in shape occurs when the waves enter the ice, and the background spectral components diminish. A distinct rotation with respect to the previous subscenes can be noticed in subscenes 3 and 4 of panel b; this is probably due to the intense shelf edge current shear observed at this location.

The application of the inversion algorithm to the imagettes in Figure 18b allowed us to retrieve a pancake ice thicknesses of 4.9±1.0 cm, 5.0±1.0 cm and 5.0±1.0 cm for imagettes 2, 3 and 4 respectively. Similar results were obtained by analyzing another northern (parallel and contiguous) strip of imagettes extracted from the same CSK image (Fig. 18a). The application of the inversion procedure on these spectra gave a thickness of 6.5±1.0 cm for the observed pancake ice (imagette 3); our method was not applied for subscene 4 where no pancake ice was identified.

These values were compared to the pancake samples collected during the buoy recovery operations on the same day, and the visual observations and thermodynamically derived ice thicknesses along the ice edge for that day (Fig. 16d, 16-24 UTC Nov 1 (hours 40-48)). The pancake measurements collected in the six recovery locations reported an average thickness of 9.6±3.8 cm (Fig. 19, Fig. 16d). Nonetheless, this value decreases to 6.7±0.6 cm when considering only the three sites located inside the window 3 of Figure 18a. The visual thickness estimates (average 5.3±0.7 cm) were similar to the sample thicknesses, while the thermodynamically-derived values were less. Hence, an excellent agreement was found between the SAR-derived estimations and both the sample and visual observations.

3.4.1 Sentinel-1 SAR-C image analysis

The inversion procedure to retrieve sea ice thickness was applied also to an Interferometric Wide Swath S1 SAR-C image (IW mode) obtained on November 1st at 17:23:26 (Fig. 20). This was a specific acquisition requested from the European Commission and ESA, instead of the usual Extended Wide (EW mode) swath usually used in this region, in order to take advantage of *Sikuliaq* in situ experiments for the validation of new methods to estimate waves and ice parameters from SAR imagery [Ardhuin et al., 2017].

The inversion procedure developed for CSK images was set up in order to be applicable for the S1 product. A wind speed of 10 m/s was considered as well as an incoming wave direction corresponding to that clearly seen in the SAR-C derived subscenes. Pancake ice thicknesses ranging from 9 cm to 41 cm were retrieved in the analyzed imagettes (Fig. 21). The results show a clear correspondence between thickness estimations, SAR spectra shape and observed ice features. This implies that more reliable values (9 cm to 16 cm) are retrieved where homogeneous pancake icefields are observed (i.e., imagettes 2 to 4 in Fig. 20); it is more difficult to obtain a confident estimate when the pancake ice is mixed with large floes, leads and fragmented ice, thus presenting a more complex spectrum to analyze, simulate and fit to the algorithm. Thus, the analysis of imagettes a-, b- and c-5 (see spectra in Fig. 21) provided ice thickness values ranging from 29 cm to 41 cm which are not consistent with ground truth.

The increase in the retrieved thickness as a function of distance from the ice edge is borne out by the *in situ* observations. While the observations at 16-24 UTC Nov 1 were along the ice edge, the observations near 02 UTC Nov 1 and 3 UTC to 9 UTC on Nov 2 (hours 26 and 51-57 in Fig. 16d, respectively) were acquired 15-20 km into the ice. These measurements show thicknesses up to 30 cm. Direct samples collected in this area report pancake values ranging from 10 cm to 18 cm and an average thickness of 11.7 cm (Fig. 19b) for the closest *in situ* measurements, while ASSIST observations reported an average thickness of 12.5 cm in this area, with single values ranging from 5 cm to 15 cm.

3.5 Algorithm accuracy and sensitivity tests

Previous studies estimated that the applied inversion procedure for the SAR-based ice thickness retrieval has an inherent accuracy of ± 1 cm [Wadhams et al., 2002, 2004]. Still, it is reasonable to consider that the algorithm is also subject to additional errors deriving from the conversion of the SAR spectrum into directional sea spectrum, the imaging process, the smoothing of the SAR spectra noise, and the input parameter accuracy. Wind is a primary input for the whole sequence of analysis. During these experiments we had the opportunity to use *in situ* wind measurements collected aboard the *Sikuliaq*, but for routine application of the method other remote wind vector sources are mandatory (i.e. satellite or model information) for a reliable inversion result.

A short test has been made to evaluate the inversion procedure general sensitivity to wind speed. Three of the experiments described above were considered; random wind speeds, ranging from 2.5 m/s to 20 m/s, were included as input in the inversion procedure for each of the experiment. Results are presented in Figure 22, where diamonds identify the ice thicknesses retrieved using the actual wind speed values measured aboard the *Sikuliaq* cruise. As expected, a clear relationship exists between wind speed and ice thickness for a given spectrum interpretation, thus having reliable wind speed estimation is of high importance when applying the inversion procedure. The dependence is especially strong for winds under 5-8 m/s. The method looks quite stable for winds over 5 m/s whilst unreliable thicknesses are retrieved when the speed falls under this threshold. There is no application for wind speeds under 2.5 m/s.

These results confirm that i) a wide range of wind classes are useful for using SAR spectra to derive the change in wave dispersion as a wave enters a pancake icefield and then derive its thickness; ii) the accuracy of the input wind parameters is essential to retrieve reliable results, especially for winds under 5-8 m/s.

4. Conclusions and discussion

We have refined and developed our original method for SAR-waves analysis of pancake icefield thickness, as originated by Wadhams, Holt and Parmiggiani during 1991-2004, to make it relevant to the new generation of SAR satellites, specifically the Italian CSK satellite cluster. In addition we have carried out a field validation study of unprecedented magnitude and complexity, which shows that the thickness estimation technique works well, and yields credible thickness values combined with consistent values for kinematic viscosity (0.03 to 0.05 $m^2\ s^{-1}$), These are also consistent with a previous validated experiment in the Antarctic [Wadhams et al., 2004].

From the cases reported here, most of which involve CSK, there is broad agreement between observed thicknesses and those retrieved from the SAR. In the case of November 1 2015 the agreement is excellent (SAR retrievals 4.9, 5.0, 6.5 cm; observed mean 6.7 cm). In the cases of October 11 the SAR retrieval (21 cm) is greater than the output from observations, and this is

also true of October 23-24 when the SAR retrieval of 18.1 cm is double the observed pancake thickness of 8.7 cm. This can possibly be ascribed to the presence of large floes in the icefield, but as we have seen from photographs, it is more likely that it is the jumbled condition of the pancake icefield with effectively two layers of pancakes present which adds to the volume of ice per unit area of sea surface. In all cases, of course, the SAR-retrieved ice thicknesses are spatial averages over the area of an imagette (about 8 x 8 km) which differs from the scale of the direct sampling.

Given the overall agreement, we feel justified in saying that this technique could now be employed in making mass flux estimates from coherent icefields of frazil-pancake ice, e.g. Antarctic ice edge and Arctic coastal polynyas, though of course further validation opportunities should be sought or created. It will be especially useful to investigate the situations where the SAR shows a thicker icefield than is suggested by the thicknesses of solitary pancakes, to see whether this implies a greater mean thickness than at first implied. This would have consequences for mass flux estimates.

Acknowledgements

We acknowledge the support of the Office of Naval Research, through contract N00014-13-1-0289 of the Sea State initiative; of the European Union ICE-ARC project (Ice, Climate and Economics – Arctic Research on Change), contract 603887; and of the European Union SPICES project (Space-Borne Observations for Detecting and Forecasting Sea Ice Cover Extremes), contract 640161. We also appreciate the efforts of all participants in the Sea State field program for collecting this unique data set necessary for validation of the SAR ice-thickness technique. We especially appreciate the contributions of S. Ackley for his organization of the ASSIST measurements and B. Lund for providing the marine radar wave direction data.
Part of this work was performed at the Jet Propulsion Laboratory, California Institute of Technology, under contract with the National Aeronautics and Space Administration.

COSMO-SkyMed imagery was made available freely to F. P. thanks to the positive acceptance of two proposals by the following programs:
1. The ASI COSMO-SkyMed Open Call for Science Program: http://www.asi.it/sites/default/files/ASI_Scientific__Announcement_of_Opportunity_finale2_23feb_2015_0.pdf (Project Proposal Id 217);
2. The ESA Third Party Mission Program (https://earth.esa.int/web/guest/missions/3rd-party-missions/overview) (Project Proposal id14674).

Sentinel-1 data are available through the Copernicus Open Access Hub at https://scihub.copernicus.eu/

References

Ardhuin, F., J. Stopa, B. Chapron, F. Collard, M. Smith, J. Thomson, M. Doble, B. Blomquist, O. Persson, C.O. Collins and P. Wadhams (2017). Measuring ocean waves in sea ice using SAR imagery: A quasi-deterministic approach evaluated with Sentinel-1 and in situ data, *Remote Sens. Environ.*, **189,** 211-222.

Aulicino, G., G. Fusco, S. Kern, and G. Budillon (2014). Estimation of sea-ice thickness in Ross and Weddell Seas from SSM/I brightness temperatures, *IEEE Trans. Geosci. Remote Sens.*, **52**, 4122-4140.

Cerrone, D., G. Fusco, I. Simmonds, G. Aulicino, G. Budillon (2017). Dominant covarying climate signals in the Southern Ocean and Antarctic sea ice influence during the last three decades, *J. Clim.*, **30**, 3055-3072

Christensen, J.H. and O.B. Christensen (2007). A summary of the PRUDENCE model projections of changes in European climate by the end of this century, *Climatic Change*, **81**, 7-30.

Doble, M., G. De Carolis, M. H. Meylan., J.R. Bidlot and P. Wadhams (2015). Relating wave attenuation to pancake ice thickness, using field measurements and model results, *Geophys. Res. Lett.*, **42**, 4473–4481.

Donelan, M. A., J. Hamilton, and W. H. Hui (1995). Directional spectra of wind generated waves, *Philos. Trans. R. Soc. London*, **315**, 509–562.

Engen, G., and H. Johnsen (1995). SAR-ocean wave inversion using image cross spectra, *IEEE Trans. Geosci. Remote Sens.*, **33**, 1047–1056.

Hasselmann, K. and S. Hasselmann. (1991). On the nonlinear mapping of an ocean wave spectrum into a synthetic aperture radar image spectrum and its inversion, *Journal of Geophysical Research*, **96**, 10713– 10729.

Hasselmann, S., C. Brüning, K. Hasselmann, and P. Heimbach (1996). An improved algorithm for the retrieval of ocean wave spectra from synthetic aperture radar image spectra, *J. Geophys. Res.*, **101**, 16615–16629.

Jacobs, S.S. 2004). Bottom water production and its links with the thermohaline circulation. *Antarct. Sci.*, **16**, 427–437.

Keller, J. and M. Weitz (1950). Reflection of waves from floating ice in water of finite depth,

Comm. Pure Appl. Math., **3**, 305-318.

Keller, J. (1998). Gravity waves on ice-covered water, *J. Geophys. Res.*, **103,** 7663-7669.

Kinney, J.C., W. Maslowski and S. Okkonen (2009). On the processes controlling shelf-basin exchange and outer shelf dynamics in the Bering Sea, *Deep-Sea Res. II*, **56**, 1351-1362.

Lund, B., C.J. Zappa, H.C. Graber, and A. Cifuentes-Lorenzen (2017). Shipboard wave measurements in the Southern Ocean, *J. Atmos. Oceanic Technol.*, 34 (9), 2113-2126.

Migliaccio, M., A. Montuori and F. Nunziata (2012). X-band azimuth cut-off for wind speed retrieval by means of COSMO-SkyMed SAR data, *Baltic International Symposium*, IEEE/OES, Klaipeda, 1-4.

Morawitz, W.M.L., P.J. Sutton, P.F. Worcester, B.D. Cornuelle and J.F. Lynch (1996). Three-dimensional observations of a deep convective chimney in the Greenland Sea during winter 1988/1989, *J. Phys. Oceanogr*., **26**, 2316-2343.

Newyear, K. and S. Martin (1999). Comparison of laboratory data with a viscous two-layer model of wave propagation in grease ice, *J. Geophys. Res.*,**104** (C4), 7837-7840.

Sansiviero, M., M.Á. Morales Maqueda, G. Fusco, G. Aulicino, D. Flocco and G. Budillon (2017). Modelling sea ice formation in the Terra Nova Bay polynya, *J. Mar. Syst.*, **166**, 4-25.

Thomson, J., et al. (2015). ONR Sea State DRI Cruise Report [available at http://www.apl.washington.edu/project/projects/arctic_sea_state/pdfs/cruise_report.pdf].

Wadhams, P. (1986). The seasonal ice zone. In *The Geophysics of Sea Ice* (ed. N. Untersteiner), Proc. NATO Advanced Study Inc on Air-Sea Interaction in the Presence of Ice, Maratea, 26 Sept - 10 Oct 1981. Plenum Press, New York. 825-991.

Wadhams, P**.** and B. Holt. (1991). Waves in frazil and pancake ice and their detection on Seasat synthetic aperture radar imagery, *J. Geophys. Res.*, **96(**C5), 8835-8852.

Wadhams, P. and J. Thomson (2015). The Arctic Ocean cruise of R/V *Sikuliaq* 2015. An investigation of waves and the advancing ice edge, *Il Polo*, **LXX**(4), 9-52 (in English and Italian).

Wadhams, P**.** and J.P. Wilkinson (1999). The physical properties of sea ice in the Odden ice tongue, *Deep-Sea Res. II*, **46**, 1275-1300.

Wadhams, P., M. A. Lange and S. F. Ackley (1987). The ice thickness distribution across the Atlantic sector of the Antarctic Ocean in midwinter, *J. Geophys. Res.*, **92**(C13), 14535-14552.

Wadhams, P., F. Parmiggiani, G. de Carolis and M. Tadross (1999). Mapping the thickness of pancake ice using ocean wave dispersion in SAR imagery. In *The Oceanography of the Ross Sea, Antarctica* (eds. G. Spezie and G.M.R. Manzella). Springer-Verlag, Milan, 17-34.

Wadhams, P., F. Parmiggiani and G. de Carolis (2002). The use of SAR to measure ocean wave dispersion in frazil-pancake icefields, *J. Phys. Oceanogr.*, **32**, 1721-1746.

Wadhams, P., F. Parmiggiani and G. de Carolis, D. Desiderio and M.J. Doble (2004). SAR imaging of wave dispersion in Antarctic pancake ice and its use in measuring ice thickness, *Geophys. Res. Lett*. **31**, L15305.

Wadhams, P., G. Budeus, J. P. Wilkinson, T. Loyning and V. Pavlov (2004). The multi-year development of long-lived convective chimneys in the Greenland Sea, *Geophys. Res. Lett.*, **31**, L06306.

Wadhams, P., G. Aulicino, F. Parmiggiani and L. Pignagnoli (2016). Sea ice thickness mapping in the Beaufort Sea using wave dispersion in pancake ice – a case study with intensive ground truth, European Space Agency Special Publication, *ESA SP*, SP-740.

Wang, X., J. R. Key and Y. Liu (2010). A thermodynamic model for estimating sea and lake ice thickness with optical satellite data, *J. Geophys. Res.*, **115**, C12035.

Yu, Y. and D. A. Rothrock (1996). Thin ice thickness from satellite thermal imagery, *J. Geophys. Res.*, **101**, C10, 25753-25766.

Figures and Tables

Figure 1

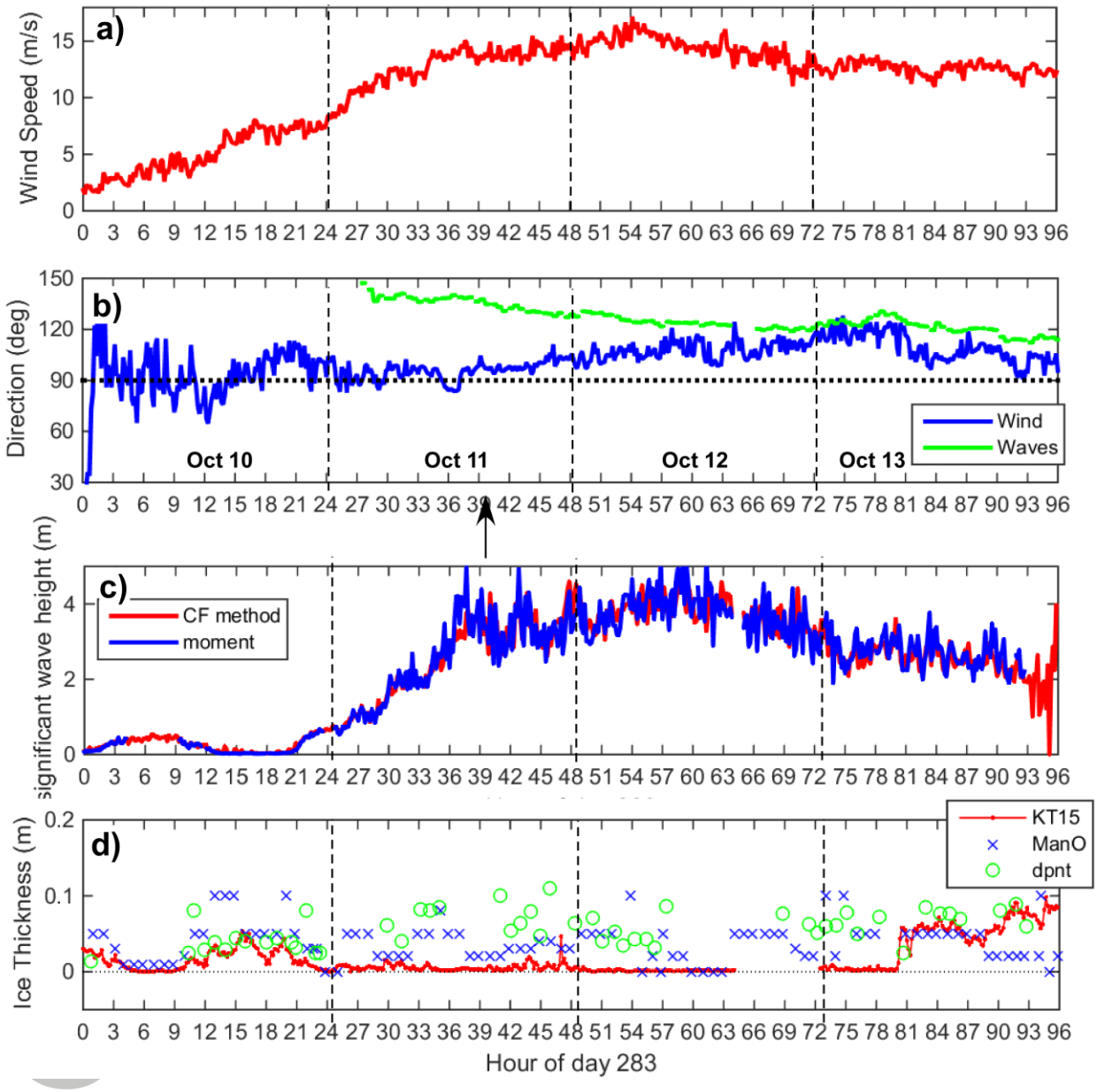

Figure 1. Time series Oct 10 through Oct 13 of a) 16-m wind speed; b) wind and wave directions; c) significant wave height from the 1-D lidar (calculated by two methods); and d) ice thickness estimates from the thermodynamic technique (KT15), ASSIST protocol (ManO), and the dipnet sampling (dpnt). The arrow marks the time of the SAR acquisition, while the vertical dashed lines separate days. Wave directions are from the shipboard marine radar processed as in Lund et al. [2017].

Figure 2

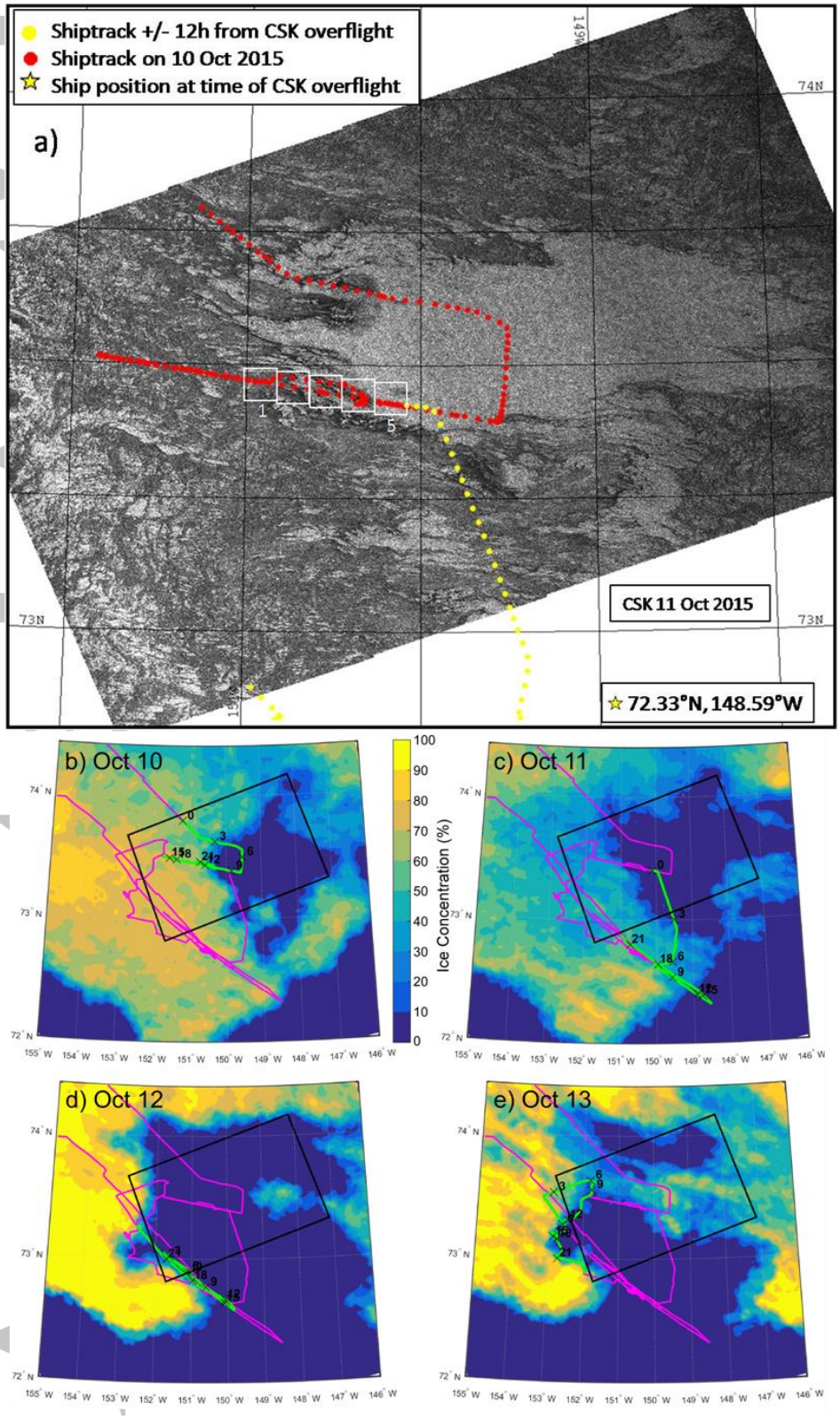

Figure 2. a) Area of *Sikuliaq* field operations seen from CSK SAR-X on October 11 at 1434 UTC and AMSR2 ice concentration and the *Sikuliaq* ship track on b) Oct 10, c) Oct 11, d) Oct 12, and e) Oct 13. In a) the white area is open water; the pancake ice (dark filaments) to S and SE are very recent, as until Oct 10 the open water was part of a completely open sea extending to the Alaska coast. *Sikuliaq* ship track (red and yellow dots) and position at time of satellite overflight (yellow star) are indicated; white rectangles identify the imagettes analyzed along the extracted stripmap. In b)-e), the magenta line shows the ship track within the domain, the green line shows the ship track on the day for which the AMSR2 data is valid, and "x" shows the location of the ship at the given hour of that day. The black rectangle shows the domain of the 1434 UTC Oct 11 SAR image.

Figure 3

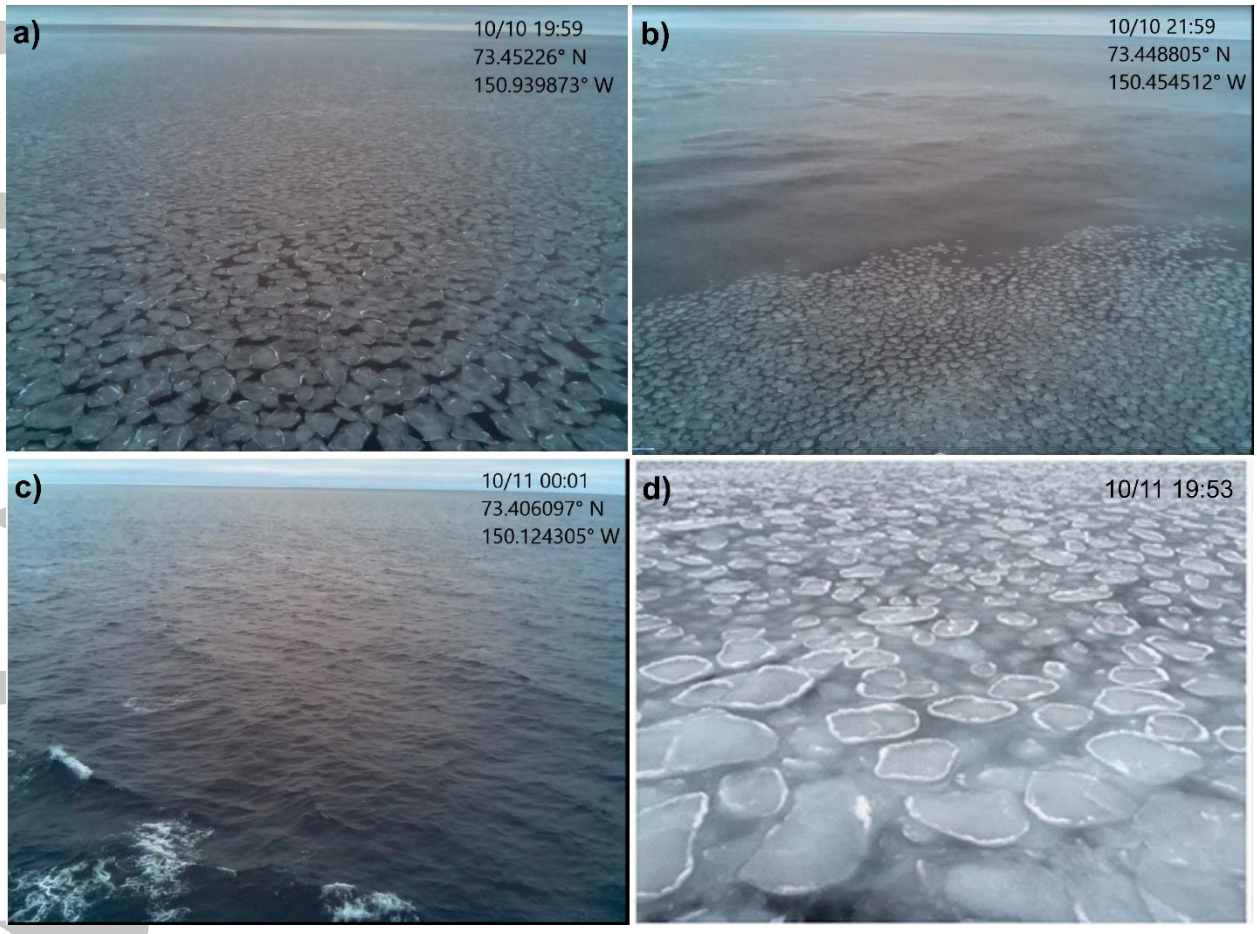

Figure 3a-c. The state of pancake ice along the northern track in Fig. 2 on Oct 10, showing the surface approximately corresponding to SAR imagettes 2, 4, and 5, respectively, sampled the following day. Fig. 3d shows the pancake ice along the southern track at 1953 UTC after strong winds and significant waves had been acting on the ice for over 12 h. This image shows the double-layered pancake ice discussed in text (image 3642, *Sikuliaq* data file). S. Ackley provided panels a)-c) from his onboard photographic record.

Figure 4

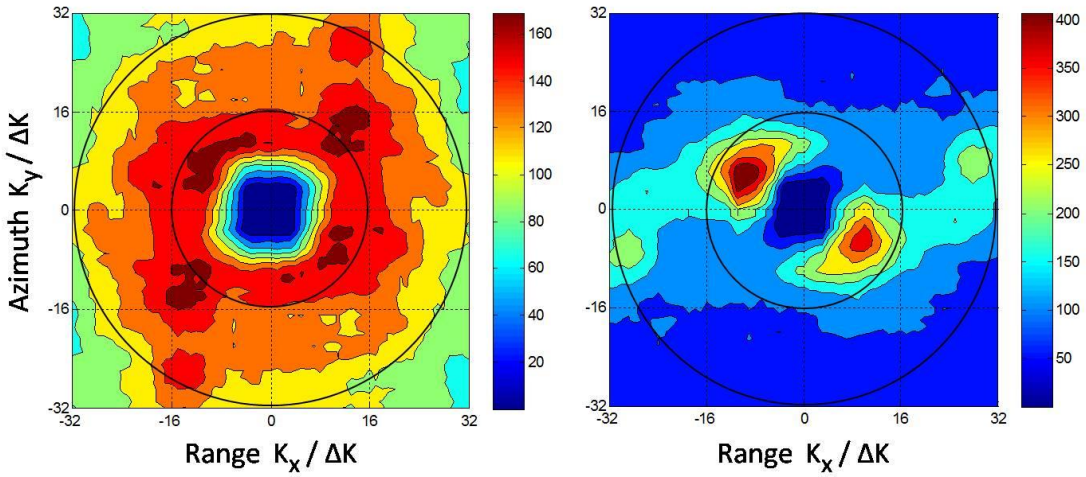

Figure 4. Observed SAR spectra for (left) open water (imagette 5) and (right) sea-ice (imagette 3) extracted from CSK SAR-X on October 11. Units are wavenumber $K_x/\Delta K$ and $K_y/\Delta K$, with $\Delta K = \pi/8\ 10^{-2}$ rad m^{-1}; the black circles correspond to λ = 50 and 100 m, from the outer to the inner respectively.

Figure 5

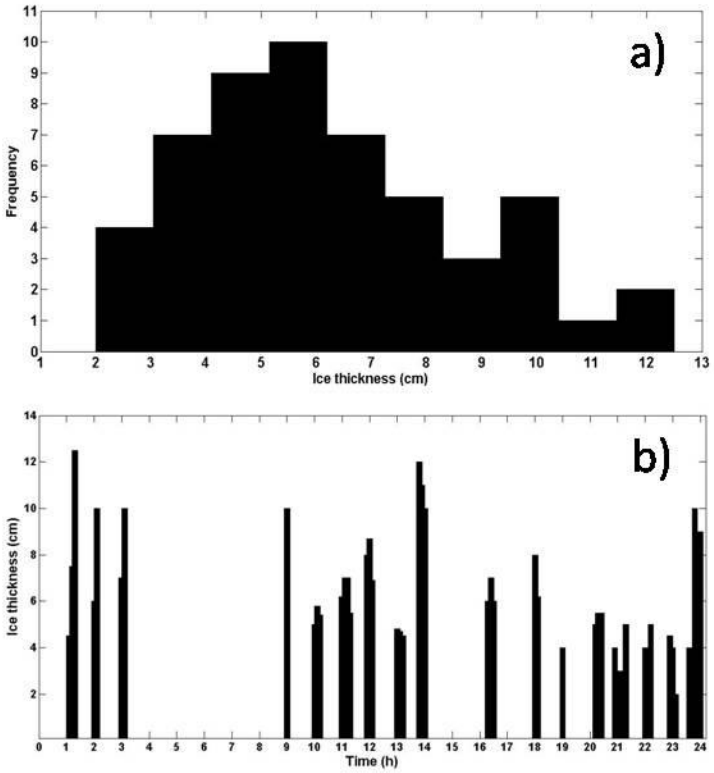

Figure 5. a) Distribution and b) temporal evolution of the measured thickness (cm) of pancake samples collected on the 11th October during the *Sikuliaq* experiment at the SAR-observed site.

Figure 6

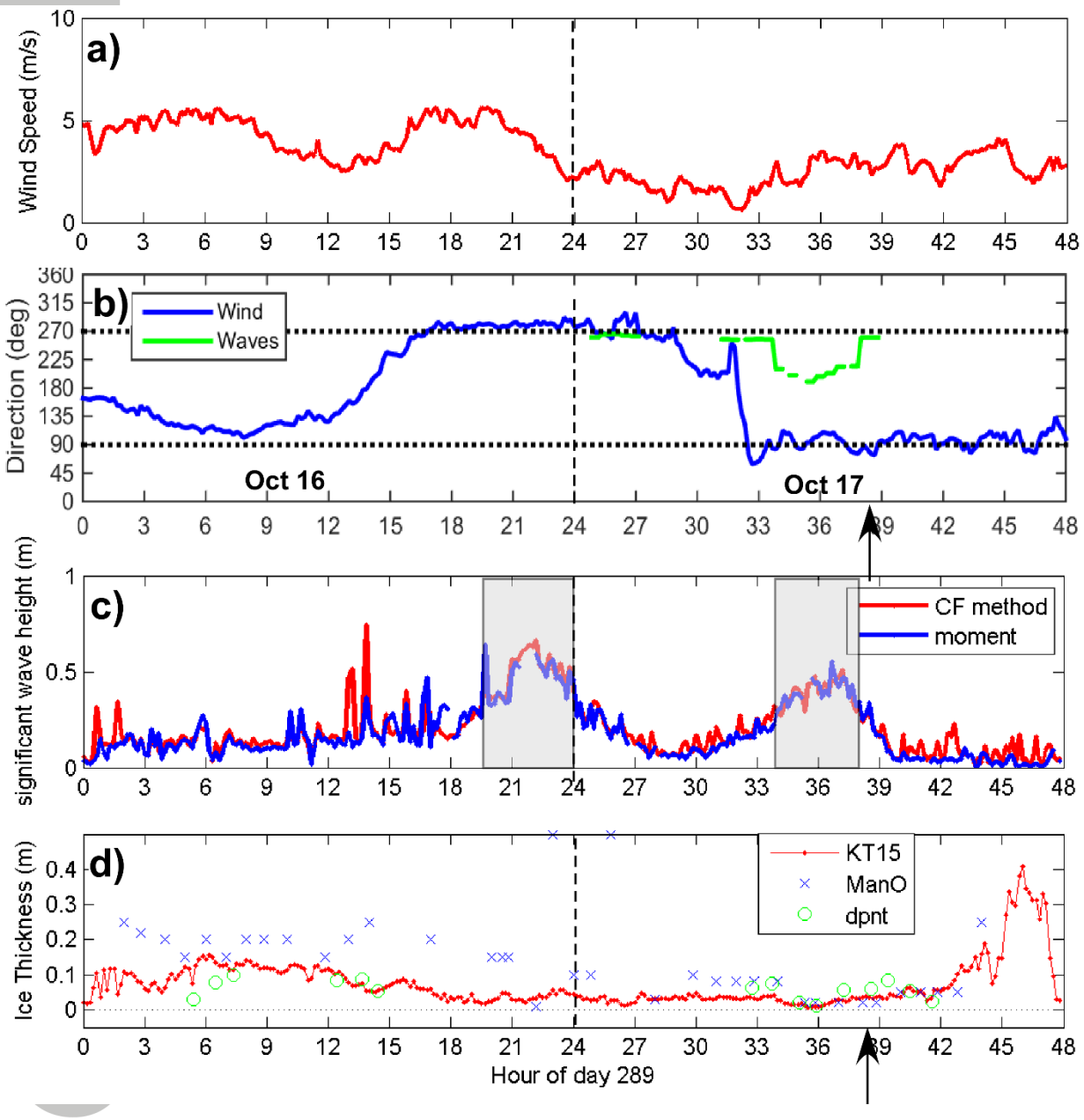

Figure 6: Same as Fig. 1, but for Oct 16-17. The shading in c) indicate times when the ship was in very low ice concentration and the arrows mark the time of the SAR acquisition.

Figure 7

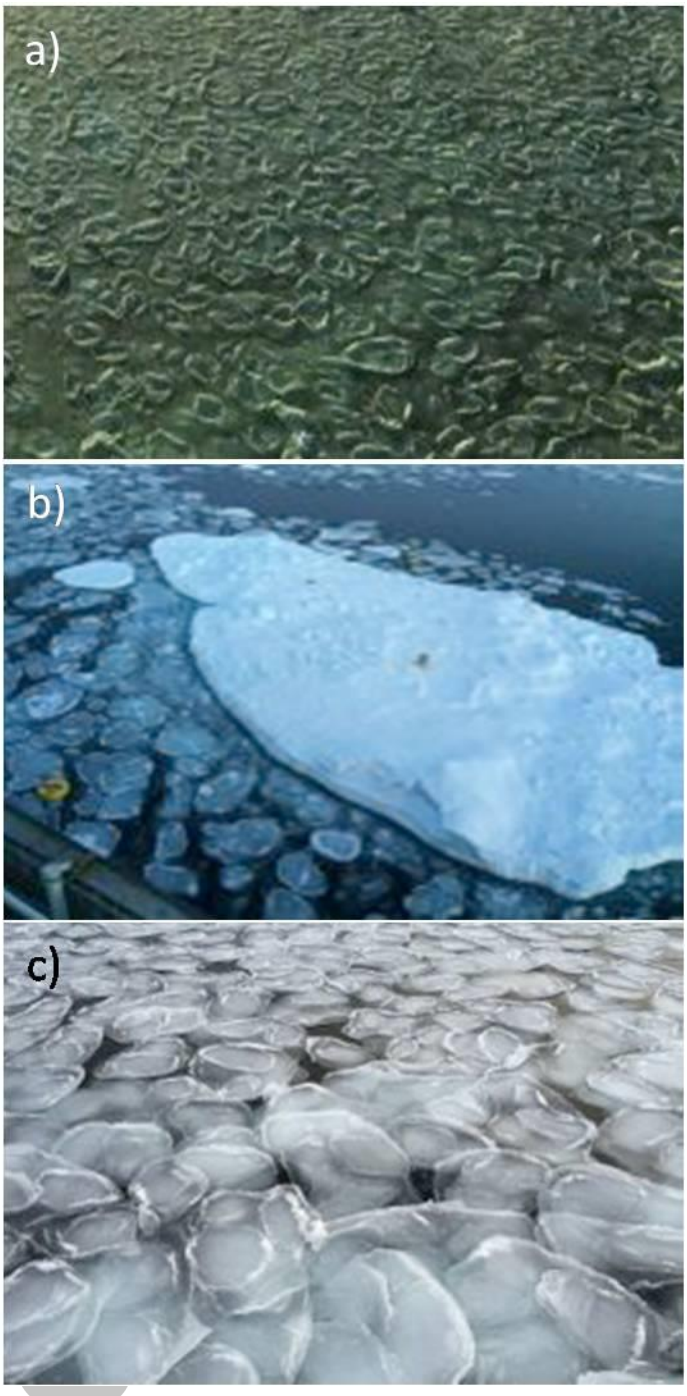

Figure 7. a) The state of pancake ice during the 16-17 October experiment; b) a multi-year ice floe heaving amongst the pancakes, and c) the pancake ice on October 18th .

Figure 8

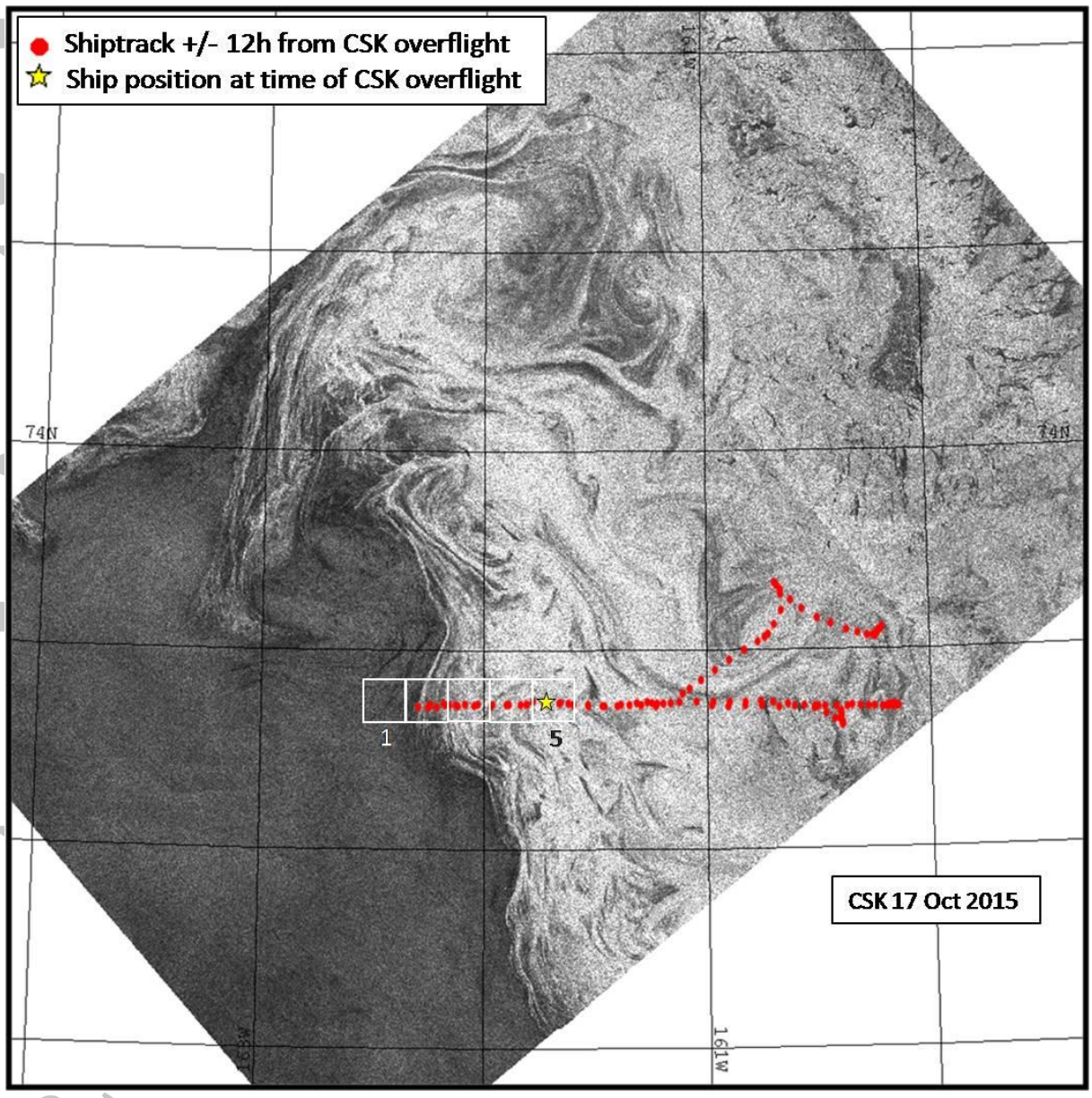

Figure 8. Area of *Sikuliaq* field operations seen from CSK SAR-X on October 17. Note eddy structure.

Figure 9

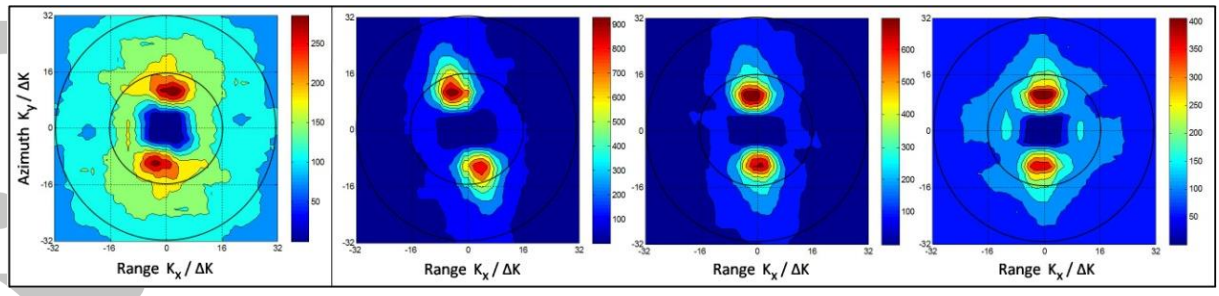

Figure 9. Observed SAR spectra for (left) open water (imagette 1) and (right) sea-ice (imagettes 3 to 5 respectively) extracted from CSK SAR-X on October 17. Units and details as in figure 4.

Figure 10

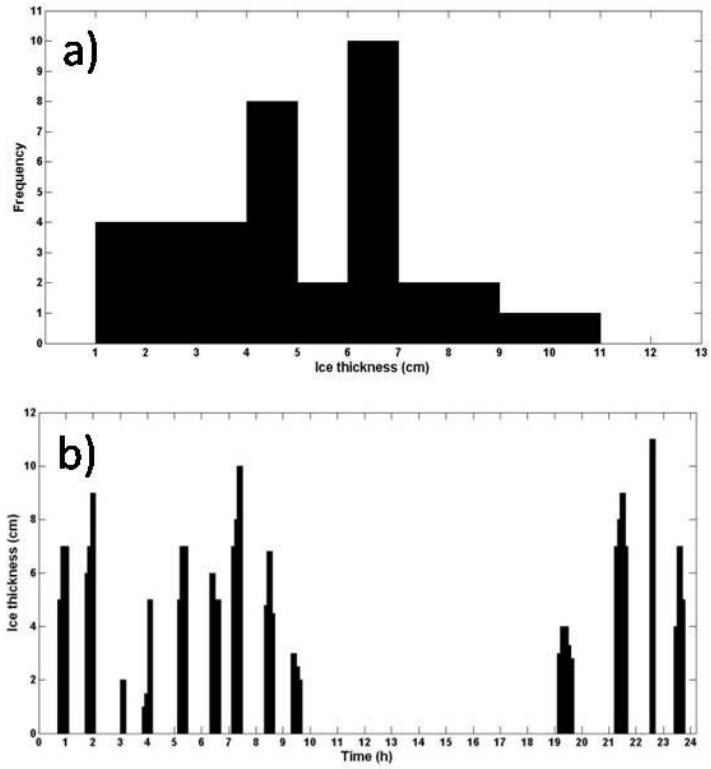

Figure 10. a) Distribution and b) temporal evolution of the measured thickness (cm) of pancake samples collected on the 17th October during the *Sikuliaq* experiment at the SAR-observed site.

Figure 11

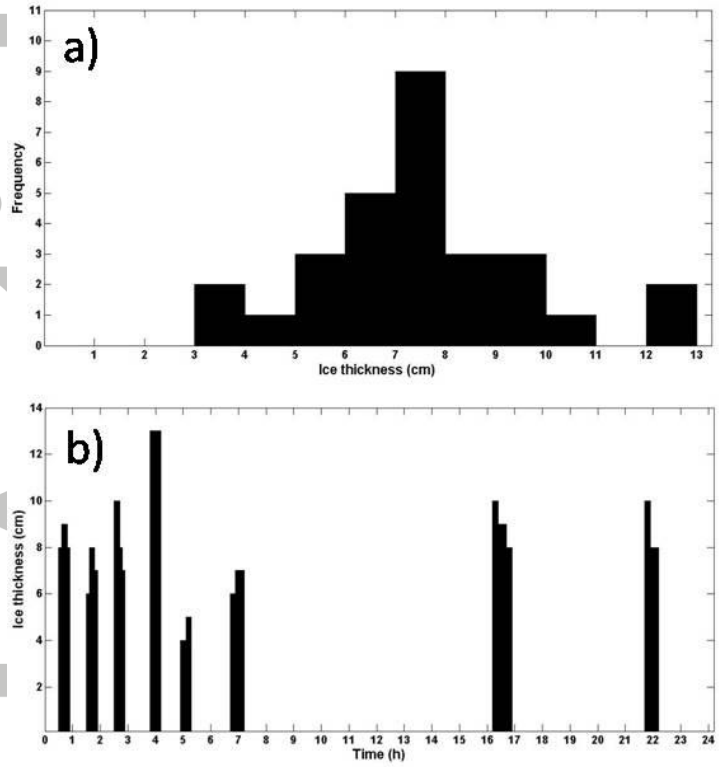

Figure 11. a) Distribution and b) temporal evolution of the measured thickness (cm) of pancake samples collected on the 18th October during the *Sikuliaq* experiment at the SAR-observed site.

Figure 12

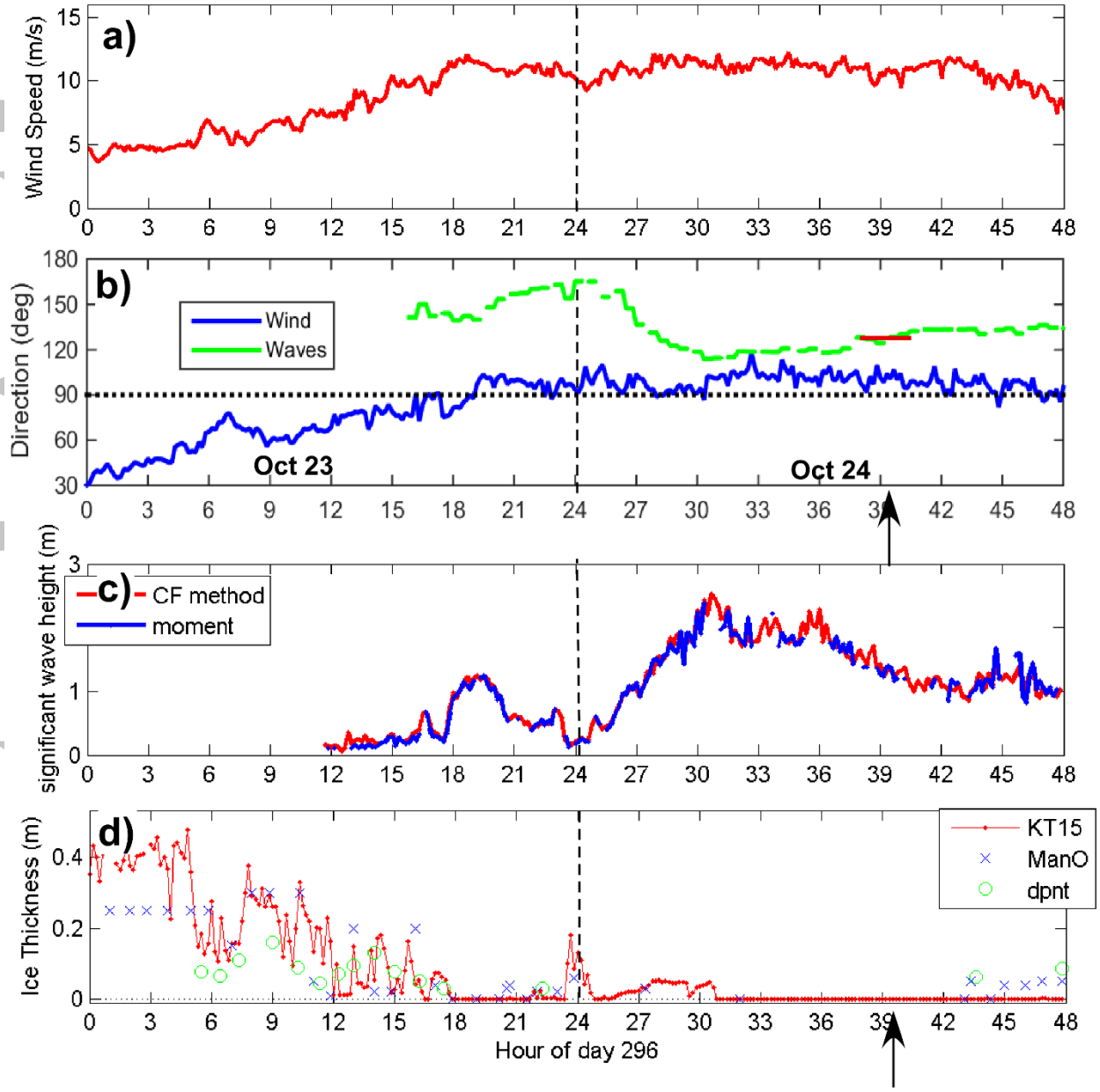

Figure 12: As for Fig. 1, except for Oct 23-24. The short red line in b) shows the orientation of the ice edge near the ship based on AMSR2 data for Oct 24.

Figure 13

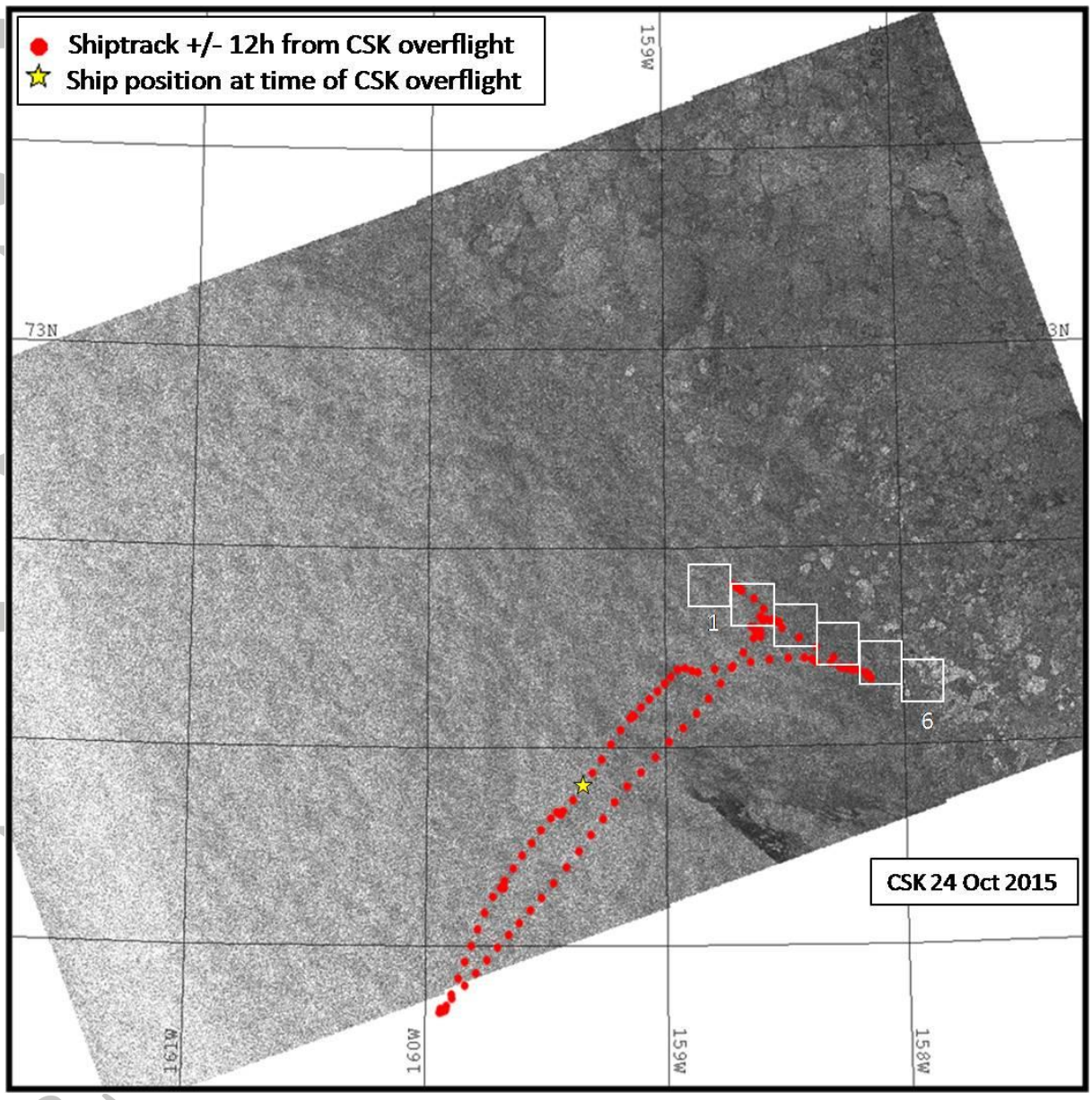

Figure 13. Area of *Sikuliaq* field operations seen from CSK SAR-X on October 24.

Figure 14

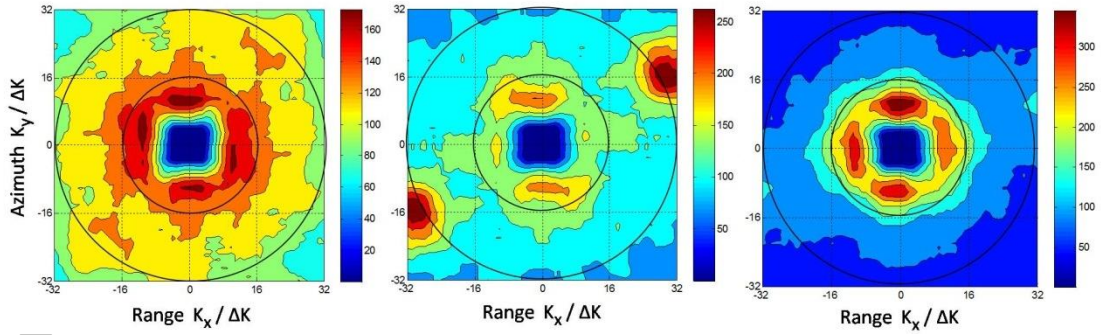

Figure 14. Observed SAR spectra for (left) open water (imagette 2) and (right) sea-ice (imagette 5 and 6) extracted from CSK SAR-X on October 24. Units and details as in figure 4.

Figure 15

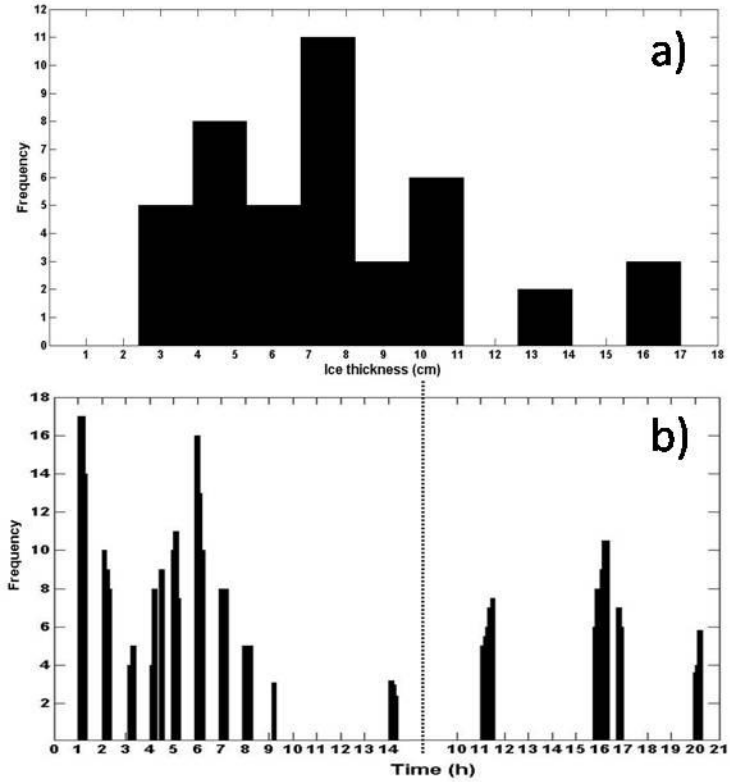

Figure 15. a) Distribution and b) temporal evolution of the measured thickness (cm) of pancake samples collected on the 23rd and 24th October during the *Sikuliaq* experiment in the region observed by SAR.

Figure 16

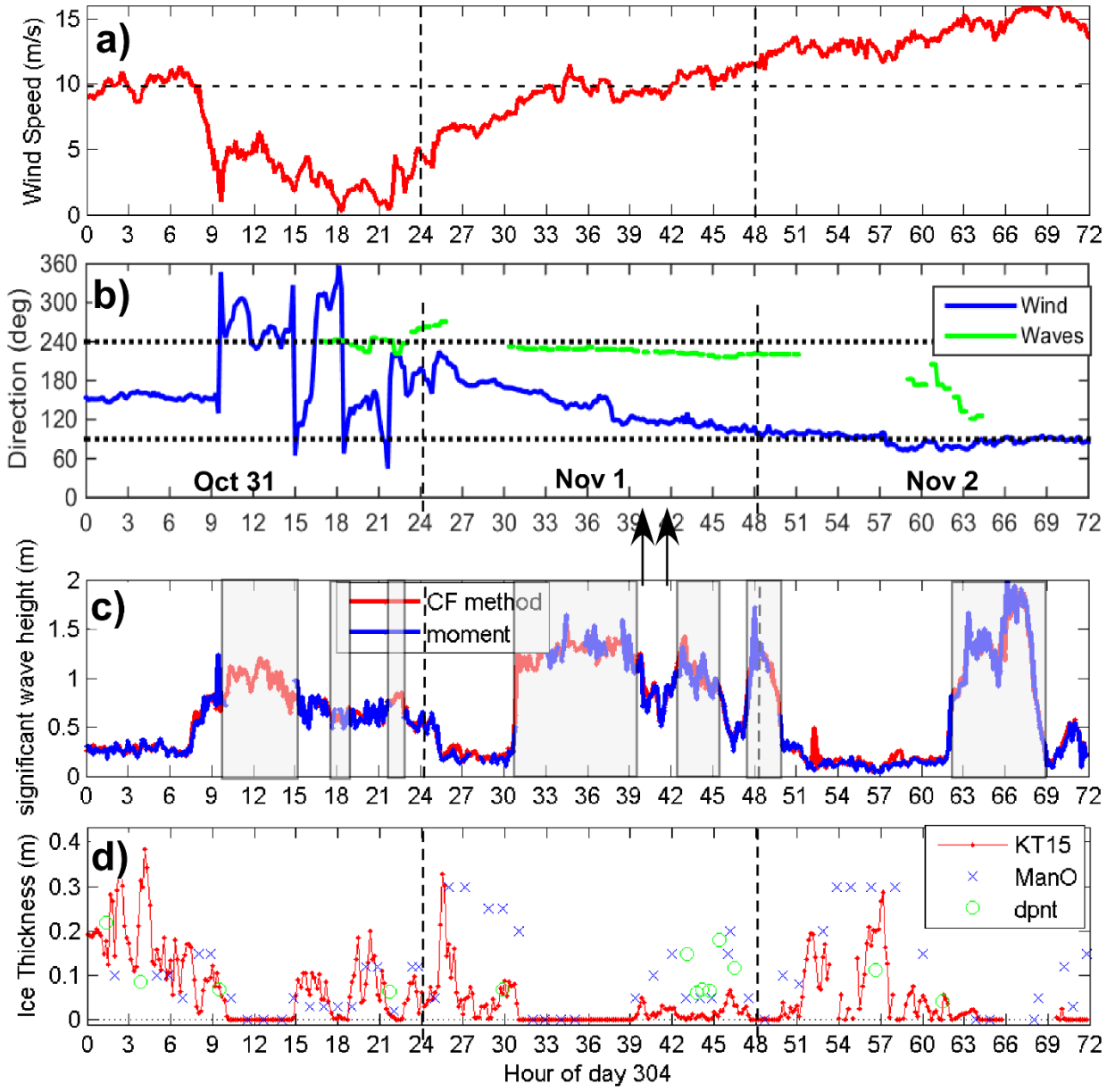

Figure 16: As in Fig. 1, but for Oct 31 through Nov 2. The shaded areas in c) show times when the ship was in low or zero ice concentration.

Figure 17

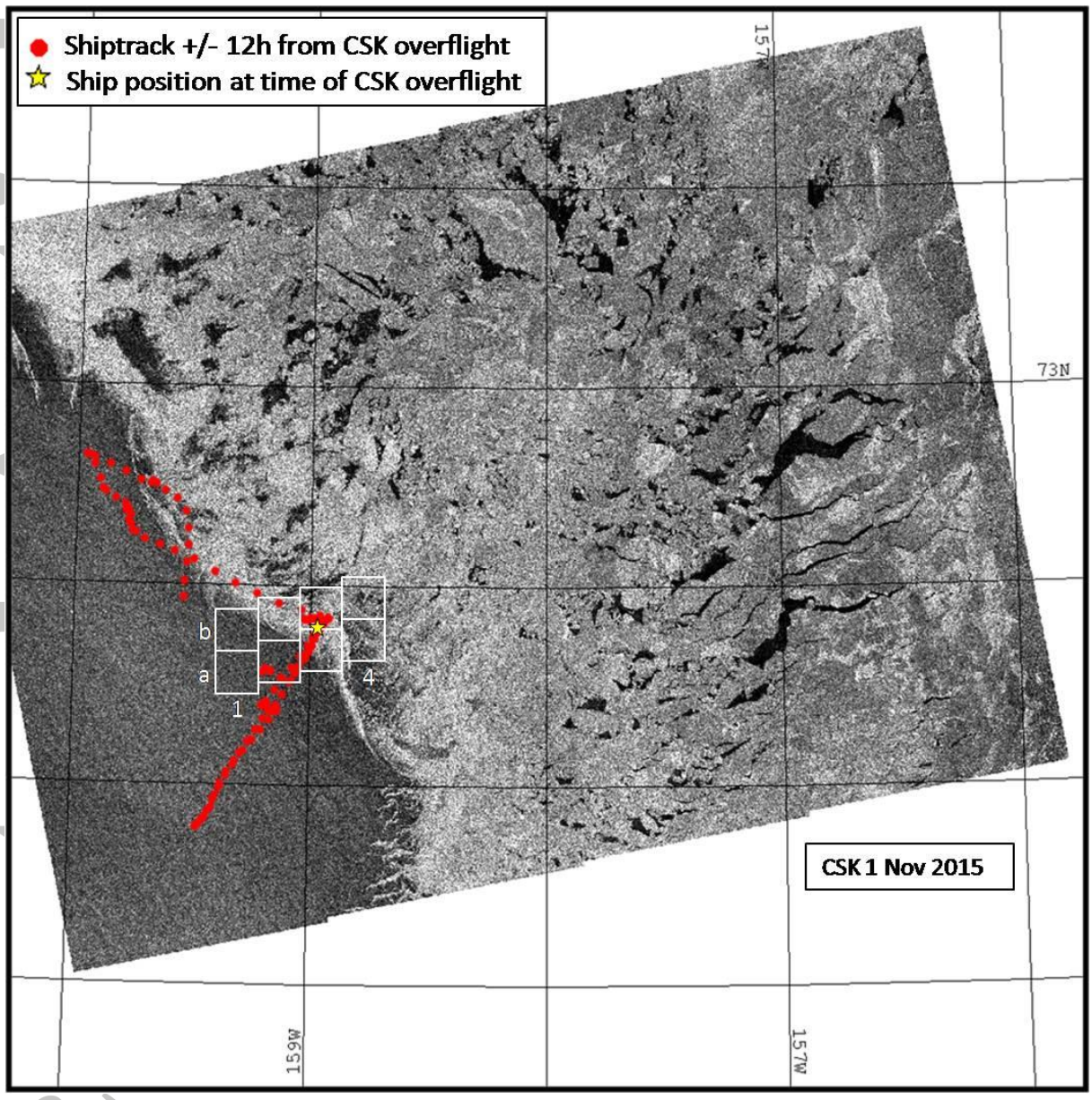

Figure 17. Area of *Sikuliaq* field operations seen from CSK SAR-X on November 1.

Figure 18

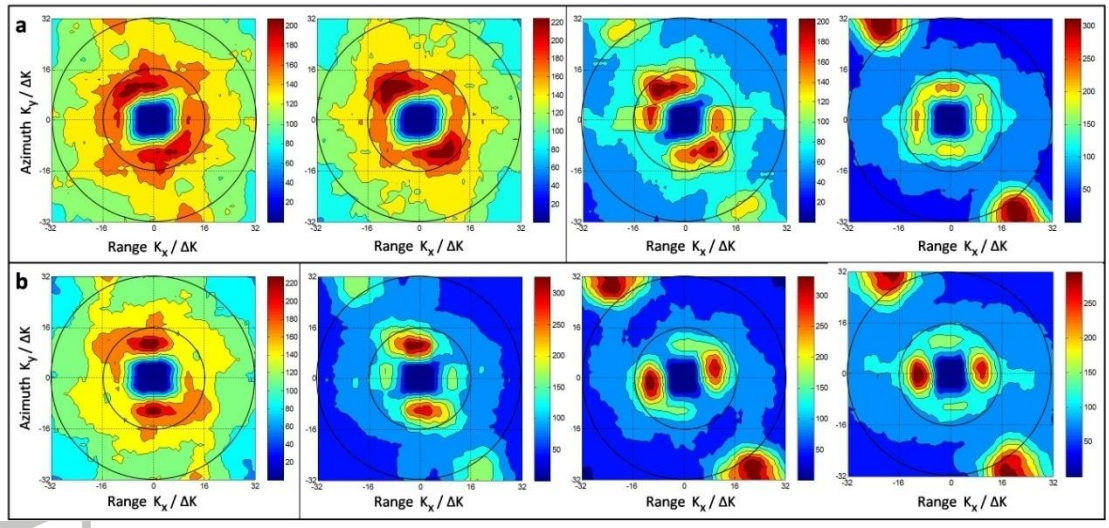

Figure 18. Observed SAR spectra for (left) open water and (right) sea-ice extracted from CSK SAR-X on November 1. Units and details as in figure 4.

Figure 19

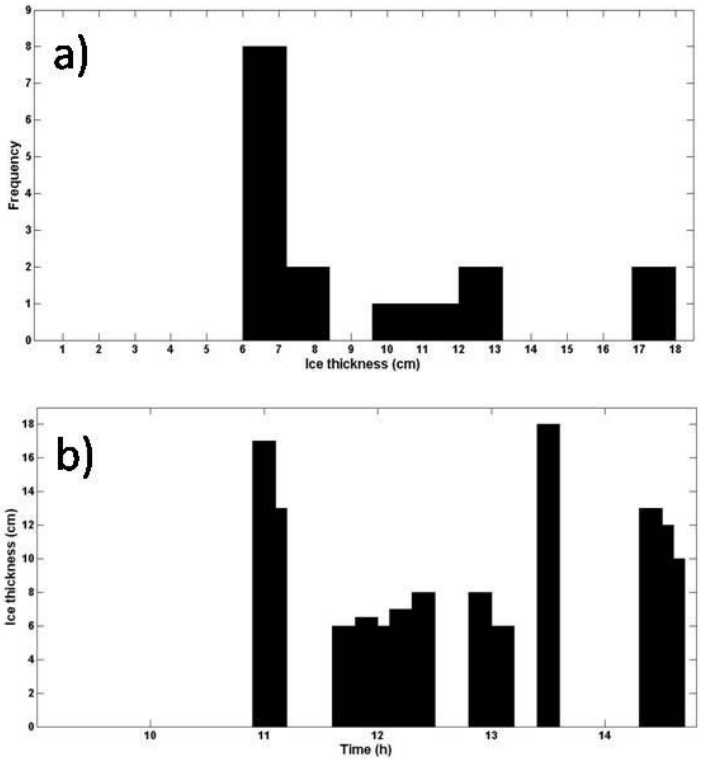

Figure 19. a) Distribution and b) temporal evolution of the measured thickness (cm) of pancake samples collected on the 1st November during the *Sikuliaq* experiment in the region observed by SAR.

Figure 20

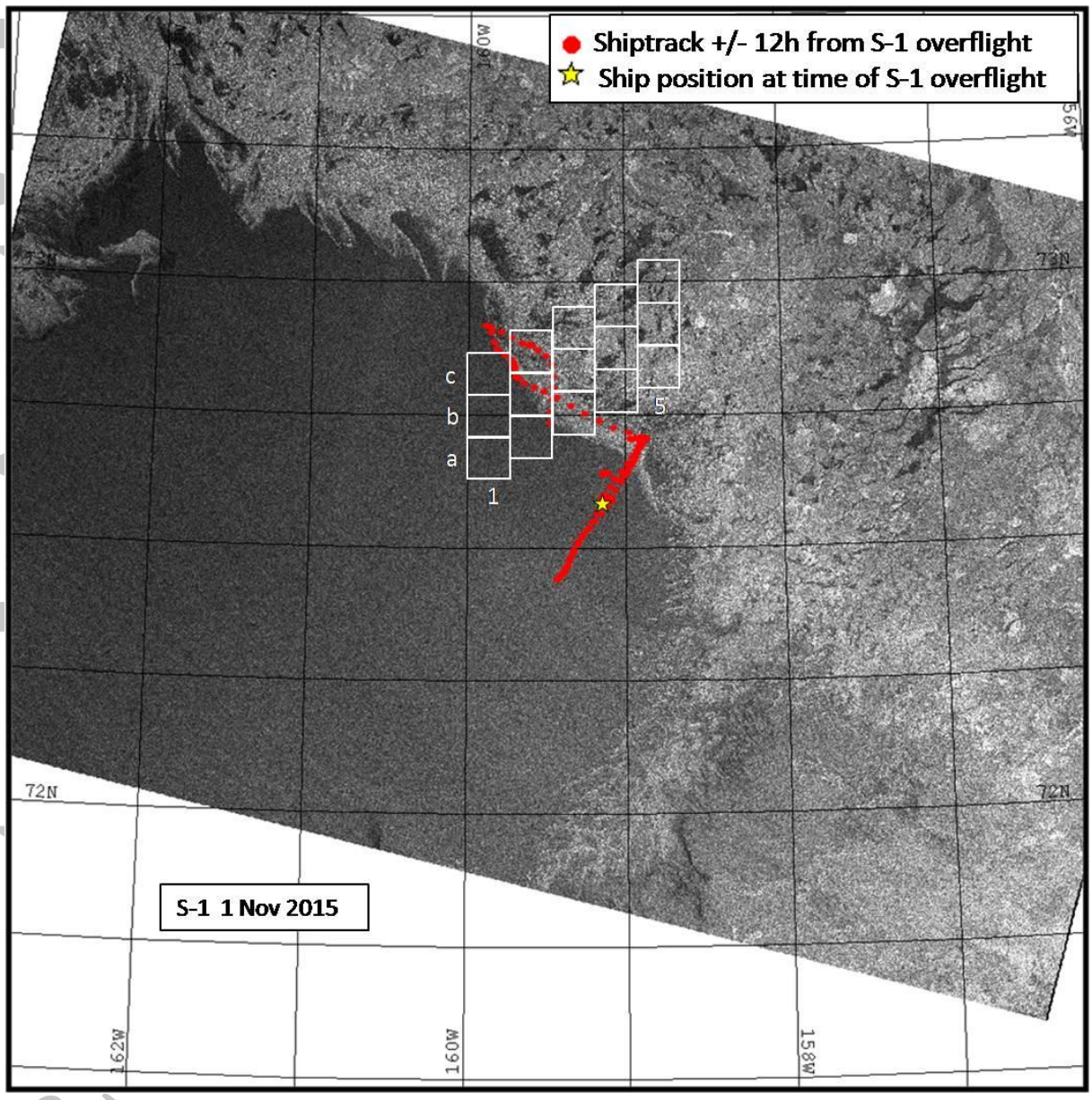

Figure 20. Area of *Sikuliaq* field operations seen from S1 SAR-C on November 1 (IW mode).

Figure 21

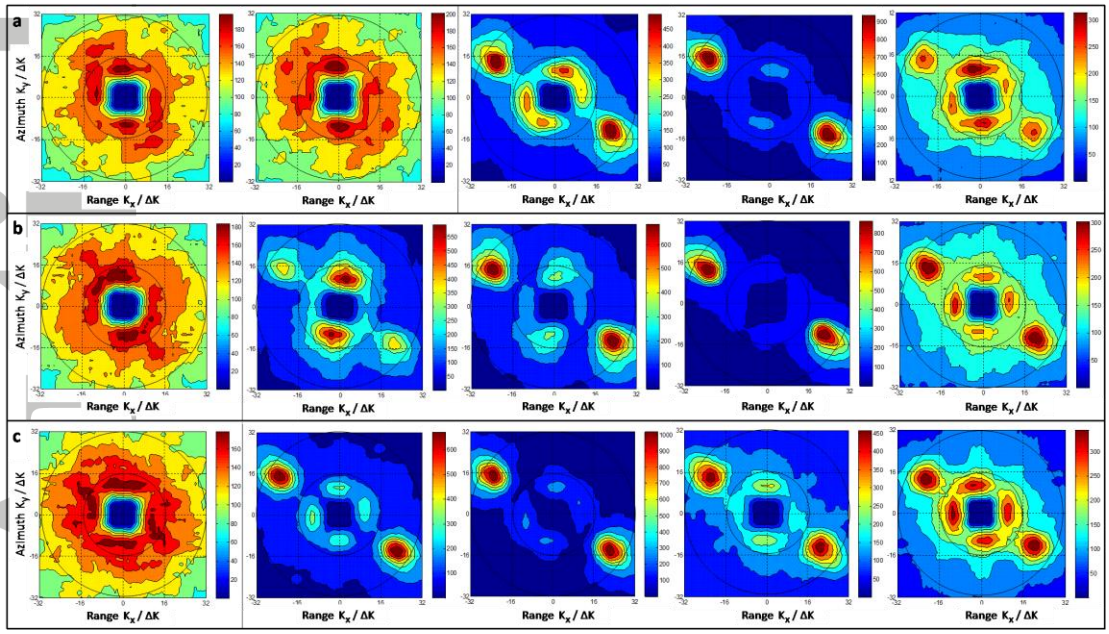

Figure 21. SAR spectra derived for three contiguous stripmaps along the sites of *Sikuliaq* field activities on November 1st. Open water (left) and sea-ice (right) subscenes can be easily identified.

Figure 22

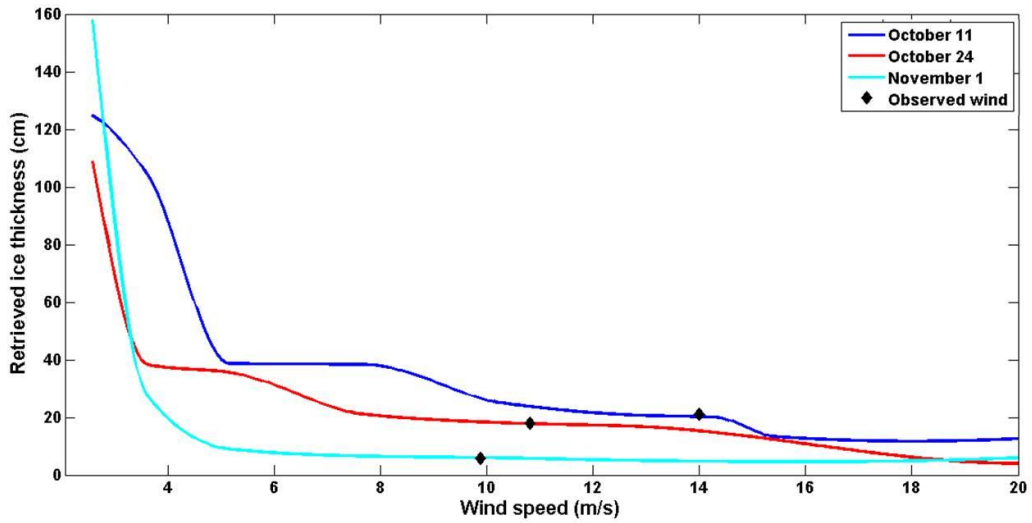

Figure 22. Inversion procedure sensitivity to random wind speeds (m/s) for October 11th (blue), October 23rd (red) and November 1st (cyan) case studies. Diamonds identify actual wind speed values measured aboard the *Sikuliaq* cruise.

Table 1

Location	Description
Site 1	Large, layered whole pancake retrieved, 85 x 63 cm, 17 cm thick. Two layers (rafting) melted separately.
Site 2	Whole pancake retrieved, 40x32 cm, 6 cm thick which included a 2-3 cm raft. So pancakes much thinner than first site.
Site 3	Frazil ice sample plus pancake 38 x 48 cm, 7 cm thick.
Site 4	Brash fragments 3-6 cm thick while largest pancake piece recovered was 28x21 cm, 8 cm thick.
Site 5	Piece of pancake retrieved was 18 cm thick, hard ice.
Site 6	Dense large single pancakes with rims, frazil and brash in between. Frazil collected and a 12 cm thick pancake, hard ice.

APPENDIX A – Spectral inversion of the SAR image in open water

For open water subscenes, the applied inversion procedure first estimates the wind-sea spectrum following the parameterisation suggested by Donelan et al. [1995]. The wind information, provided through the *Sikuliaq* in situ measurements, are used to compute the wave age value $\Omega = C_p/U_{10}$, where C_p is the phase speed of the peak wave which minimizes the difference between the observed and simulated SAR spectra. The simulated two dimensional SAR spectrum is derived through the non linear integral transform suggested by Hasselmann and Hasselmann [1991], as improved by Hasselmann et al [1996]. To this aim, a preliminary estimation of the real aperture radar (RAR) modulation transfer function (MTF) was performed on the SAR image, expressed as the slope $(\delta\sigma/\delta\theta)/\sigma$, where σ is the backscatter coefficient and θ is the incidence

angle. The inversion scheme involves the minimization of a properly defined cost function *J*, which uses the observed SAR spectrum $P_0(\mathbf{k})$, the first guess ocean directional wave spectrum $F_0(\mathrm{k})$ and the SAR spectrum computed from the best fit ocean wave spectrum $F(\mathbf{k})$, as follows:

$$J = \int d\mathbf{k}\,[P(\mathbf{k}) - P_0(\mathbf{k})]^2 \cdot P_0(\mathbf{k}) + \mu \int d\mathbf{k} \left\{ \frac{F(\mathbf{k}) - F_0(\mathbf{k})}{B + \min[F(\mathbf{k}), F_0(\mathbf{k})]} \right\}^2 + \eta \frac{\upsilon \lambda^2 - {\lambda_0}^2}{max(\lambda^4 - {\lambda_0}^4)} \qquad (1)$$

where λ_0 and λ are the clutter cut-off length of the observed and simulated SAR image; ν minimize the error between simulated and observed spectra; B, μ and η are constants needed to prevent the denominator from vanishing, and minimize the impact on results, respectively. In this study, we assumed the following values for these constants:

$$B = F_{0\,max}\, 10^{-3} \qquad (2)$$

$$\mu = P_{0\,max}\, 10^{-2} \qquad (3)$$

$$\eta = 5 \cdot 10^4 [\int P_0(\mathbf{k})\, d\mathbf{k}]^3 \qquad (4)$$

Note that the SAR spectrum $P(\mathbf{k})$ is here computed by fast Fourier transform as

$$P(\mathbf{k}) = e^{(-{k_x}^2 \cdot \xi^2)} \sum_{n=1}^{\infty} \sum_{m=2n-2}^{2n} (k_x \beta)^m\, P_{n,m}(\mathbf{k}) \qquad (5)$$

where β = R/V is the ratio between slant range and platform velocity; k_x is the wave number component along the azimuth direction in the SAR image; $P_{n,m}$ are the products of auto and covariance functions of the slant range components of the orbital velocity and the real cross section modulation. The non linear exponential factor is related to the azimuthal cut-off and depends on ξ, i.e. the mean square azimuth displacement of a scattering element which takes into account the frequency dependence of the range velocity transfer function. This cut-off is based on the fact that the orbital motions of sea surface waves induce a SAR Doppler mis-registration along the azimuth direction, so that the ocean wave spectrum is not entirely mapped in the SAR imagery. This effect depends on both sensor parameters (e.g. platform altitude, velocity, etc.) and sea state conditions [Migliaccio et al., 2012] and affects the nominal along-track (azimuthal) resolution making it impossible to observe the shortest wave components [Ardhuin et al., 2017].

APPENDIX B – Spectral inversion of the SAR image in Sea Ice

A wave propagation model, based on Keller [1998], is used to invert the SAR image spectra in sea ice imagettes in order to retrieve pancake ice thickness, when present. Here, the sea ice layer is treated as a viscous fluid, the sea water beneath it being assumed as inviscid. The iterative procedure looks for the best sea ice thickness and sea ice viscosity values which minimise the difference between the observed and simulated SAR spectra. In fact, the model has only two free

parameters when dealing with deep waters. The idea is that each component of the wave spectrum is attenuated when entering the icefield. The basic relationship to account for this phenomenon and retrieve the wave spectrum in sea ice $S_{i,}$ is:

$$S_i(\mathbf{k}) = S_w(\mathbf{k}) \cdot e^{(-\alpha \cdot d)} \qquad (6)$$

where $S_w(\mathbf{k})$ is the wave spectral density in open water and α is the attenuation rate computed by the model; d is the distance travelled by the wave, from the ice edge to the centre of the sea ice subscene. The modulus of RAR MTF included in this computation comes from the procedure described in the open sea region. The parametric inversion, similar to the one implemented for open sea wave spectra, allows retrieving both thickness and kinematic viscosity at a given distance from the ice edge. The best-fit sea ice parameters allows us to compute the attenuation rate α and hence of the wave spectrum in sea ice using (6). This procedure ensures that the whole spectral shapes are matched until optimal agreement is reached, thus giving the ice thickness and the viscosity independently as results of the same optimization analysis.

Some assumptions should be taken into account when using this procedure. Firstly, we consider that energy is transmitted without loss when the waves imaged by SAR cross the ice edge; this is true while we are dealing with thin sea ice and explains why this procedure does not provide reliable results when applied to thicker ice types than pancake and frazil ice. Secondly, we assume that the amount of rotation is independent of the wavelength when these waves cross the ice edge; this feature is considered in the inversion procedure as rigid rotation of the whole spectrum.